Chemical Engineering Journal 484 (2024) 149524

Contents lists available at ScienceDirect

Chemical Engineering Journal

journal homepage: www.elsevier.com/locate/cej

Multiphase flow and reactor optimization of a 1MWth pilot-scale circulating fluidized bed for coal staged conversion

Yuxin Ge [a], Jiahui Yu [a], Junjie Lin [a,*], Shuai Wang [a], Kun Luo [a,b,*], Qinhui Wang [a], Jianren Fan [a,b]

[a] State Key Laboratory of Clean Energy Utilization, Zhejiang University, Hangzhou 310027, China
[b] Shanghai Institute for Advanced Study of Zhejiang University, Shanghai 200120, China

ARTICLE INFO

Keywords:
Coal staged conversion
Multiphase particle-in-cell
Numerical simulation
Heat and mass transfer
Circulating fluidized bed

ABSTRACT

Coal-based cogeneration technology can realize the graded utilization of energy through the graded conversion of coal. In this work, the coal staged conversion in a 1MWth pilot-scale system was numerically studied using the multiphase particle-in-cell method which features gas–solid flow hydrodynamics, heat and mass transfer, homogeneous reactions, and heterogeneous reactions. The model was verified to be reliable and accurate in modeling coal staged conversion in fluidized bed reactors. Then the operating mechanism and particle behavior during the coal staged conversion process were comprehensively discussed. Additionally, the effects of operating and structural parameters on gas–solid mixing and chemical reactions in the reactor are explored for reactor optimization. The findings indicate that as the operating temperature increases, the CH_4 concentration at the outlet of the gasifier's cyclone initially rises before declining, whereas the trend for H_2 concentration is inverse. As the particle size distribution (PSD) width becomes broader, the "core-annulus" structure of the expansion section in the dense-phase zone gradually disappears. Increasing the diameter of the expansion section in the dense-phase zone hinders the gas generation in the rare-phase zone. Increasing the diameter of the rare-phase zone significantly reduces the number of fine particles at the exit of the gasifier, and the height of the rare-phase zone can be appropriately lowered without leading to the overflow of fine particles. The change in structure size has little effect on the product gas yields at the outlet of the cyclone separator.

1. Introduction

Referring to the BP Energy Outlook 2023, coal, oil, and gas dominate the global primary energy consumption mix, with coal consumption in thermal power generation projected to rise until 2030 [1]. By 2022, China has already accounted for 56.2 % of total energy consumption [2], emphasizing the enduring significance of coal resources as a primary energy source for global economic development [3]. Historically, coal has primarily been utilized through direct combustion, pyrolysis, gasification, and liquefaction. Direct combustion represents approximately 80 % of total coal consumption. These methods have a low energy conversion rate and result in significant pollution emissions, thereby posing threats to both the environment and human health [4–6]. Thus, the development of efficient and clean coal utilization technology has emerged as an essential way to achieve the strategic objective of "carbon neutrality" when clean energy alone fails to meet immediate energy requirements for production and human livelihoods [7,8].

In contrast to individual coal utilization methods (i.e., direct combustion, liquefaction, and gasification), coal-based cogeneration technology integrates pyrolysis, gasification, combustion, and coal synthesis processes through a graded conversion approach. Volatile components in coal can be converted into synthesis gas, serving as industrial gas and raw materials for chemical purposes. In contrast, non-volatile coke can be employed as boiler fuel for steam generation in power and heat production. Multi-coupling technology exemplifies the concept of sequential energy utilization and capitalizes on the strengths inherent in each production technology pathway. Moreover, it maximizes energy utilization efficiency while minimizing energy consumption, investment, and operating costs. Consequently, it presents a viable technological solution to address energy and environmental challenges.

Zhejiang University has developed a dual fluidized bed coal staged conversion process that integrates fluidized bed pyrolysis and circulating fluidized bed (CFB) semi-coke combustion [9,10]. This process facilitates the efficient conversion of coal and is currently being applied in industrial settings. However, the multiphase flow process in a CFB is highly complex and involves intricate physicochemical phenomena such

* Corresponding authors at: State Key Laboratory of Clean Energy Utilization, Zhejiang University, Hangzhou 310027, China (J. Lin; K. Luo).
E-mail addresses: linjunjie@zju.edu.cn (J. Lin), zjulk@zju.edu.cn (K. Luo).

https://doi.org/10.1016/j.cej.2024.149524
Received 26 November 2023; Received in revised form 29 January 2024; Accepted 7 February 2024
Available online 10 February 2024
1385-8947/

as particle mixing, collision, heat and mass transfer, and complex chemical reactions [11]. The state of fluidization in a fluidized bed plays a crucial role in understanding heat and mass transfer within the reactor. Various factors, including size and shape, the geometry of the fluidized bed, and gas properties (e.g., pressure, temperature, and velocity), collectively affect the state of fluidization. Empirical methods for calculating e.g., minimum fluidization velocity, bubble formation, particle wear, and axial solids mass fraction distribution have been summarized in laboratory-scale experiments on fluidized bed reactors for decades. Experimental measurements can provide a fundamental understanding of the hydrodynamic behavior of gas–solid reactive flows though. However, it is difficult to obtain more detailed experimental data due to the harsh experimental conditions such as high temperature and pressure and/or toxic gases, and the high cost of measurement equipment [12–14].

In recent years, the rapid advancement of computer technology has enabled computational fluid dynamics (CFD) to accurately simulate multiphase flow and thermochemical behavior within fluidized bed systems. Numerical simulations make it possible to bypass the lengthy process of planning and constructing experiments, providing a rapid evaluation of local and global flow field variables (e.g., temperature, velocity, and concentration) on an industrial scale. CFD results can provide qualitative and quantitative information about real systems. Accurate simulation results are useful for designing and understanding the dynamic operation of reactors. Examples include detailed data on velocity and temperature fields, flow turbulence, heat and mass transfer, and homogeneous and inhomogeneous reactions between solid and gas phases. CFD methods can provide cost-effective insights into the hydrodynamic behavior of energy systems, process engineering applications, and chemical processes to improve and optimize process efficiency. In addition, it is possible to demonstrate the performance of systems under different operating conditions, analyze and troubleshoot risks in industrial plants, and save time and money when designing new designs [15]. This approach is therefore widely recognized as a cost-effective and efficient method for understanding, designing, optimizing, and modifying reactors within CFB pyrolysis-combustion hierarchical conversion cogeneration systems [16,17]. The main challenge faced when performing large-scale simulations of fluidized bed systems is the scale divide between the macroscale flow structure and the microscale fundamentals of gas–solid flow. A variety of mathematical models at different scales have been developed to address this problem.

Based on the treatment of the particle phase, simulation methods can be divided into two frameworks: Eulerian-Eulerian (E-E) and Eulerian-Lagrangian (E-L) [11,18]. The E-E method treats the gas and solid phases as a continuum. This simplification significantly reduces computational costs, making the E-E method widely used in simulating gas–solid flow processes in pilot and industrial-scale fluidization equipments [19–21]. However, this framework cannot obtain particle-level information due to its simplification of the real particle motion, limiting the understanding of dense gas–solid two-phase flow systems at a microscopic level [22,23]. In contrast, the E-L method utilizes the Eulerian framework to handle the gas phase as a continuous medium, while employing the Lagrangian framework to solve the solid dynamics based on Newton's law of motion. The Computational Fluid Dynamics-Discrete Element Method (CFD-DEM) and Multiphase Particle-in-Cell (MP-PIC) methods are two representations of Eulerian-Lagrangian methods [24,25]. The CFD-DEM method tracks the movement of each particle in the system, accurately solving particle collisions, and thus providing abundant particle-scale information (e.g., position, velocity, temperature, and mass) [25–27]. However, this method consumes a significant amount of computational resources and lacks the capability to model and predict large-scale pilot or industrial-scale fluidized beds that contain numerous particles [28]. Conversely, the MP-PIC method introduces a solid stress model to simplify the particle collision process and employs numerical parcels to represent a population of particles with the same parameters (i.e., density, size, and temperature). These assumptions improve computational efficiency while maintaining a balance between solution accuracy and computational cost [24,29]. The MP-PIC method is suitable for large fluidized systems with particle number typically around 1×10^{15} [30–32].

In recent years, the MP-PIC method has been widely used to study fluidized bed systems. In 2001, Patankar and Joseph [33] performed the first 3D simulation of a fluidized bed system using the MP-PIC model for a two-configuration fluidization process involving uniform gas injection at the inlet and a jet of gas at the inlet. Karimipour and Pugsley [34] evaluated the capability of the MP-PIC approach for modeling a bubbling fluidized bed with Geldart A particles using the Barracuda Virtual Reactor software. Bubble properties were extracted from the model predictions and compared with empirical correlation predictions and experiments, which showed that the MP-PIC method showed good predictability and capability. Clark et al [35] conducted an experimental and numerical study of the gas-particle flow behavior in a full-loop circulating fluidized bed carbon capture device using Barracuda Virtual Reactor software. The gas–solid flow and pressure drop behavior predicted by the simulation is in good agreement with the video recordings and measurements provided by the National Energy Technology Laboratory. In addition to cold state studies, the MP-PIC method can be well applied to fluidized bed systems containing chemical reactions. Some investigations have used the MP-PIC method to simulate the processes of coal pyrolysis and combustion in fluidized beds. Xie et al [36] utilized the 3D-MP-PIC approach to simulate a lab-scale atmospheric coal fluidized-bed gasifier with a height of 2.0 m and a diameter of 0.22 m. It was assumed that the evaporation and devolatilization occurred instantaneously. The calculated product gas compositions were shown to compare well with the experimental data. Dou [37] conducted a numerical study on a pilot-scale 50 kg/h pyrolysis reactor and optimized the structural parameters of the reactor. The influence of the pressures on the distribution of gas–solid temperatures and particle fractions was assessed. They found that increasing the pressure enhanced particle mixing and reduced the accumulation of coal at the bottom region. Zhou et al [38] developed the MP-PIC model to simulate the gas–solid flow and pyrolysis characteristics of coal in an industrial scale 500,000 tons per year pressurized injection fluidized bed reactor. They observed that the flow pattern in the pyrolysis reactor was more stable and less well-mixed as the particle size increased. Coal pyrolysis benefits from an increase in the semi-coke to coal ratio; however, this increase is limited and comes at the cost of a dramatic increase in the number of particles in the reactor. Feng et al [39] simulated the circulating fluidization process of pulverized coal particles with multiple sizes in a full-size three-dimensional (3D) multi-stage graded conversion fluidized bed gasifier. They found that raising the height of the bubbling bed led to a decrease in particle concentration above the fast bed and an increase in the content of fine particles in the upper section of the transition region.

The MP-PIC method has been widely used for the simulation of dense gas–solid flows in fluidized beds due to its computational convenience. However, most of the current simulations are limited to the numerical simulation of cold gas–solid flows [40,41], single reactors [9,38], and laboratory-scale devices [42]. The MP-PIC model employed in this study integrates the gas–solid flow, heat and mass transfer, fuel particle drying, coal pyrolysis, char gasification, combustion, and various complex homogeneous chemical reactions in the coal graded conversion process. The investigated object of this study is a pilot-scale dual circulating fluidized bed coal graded conversion system, utilizing the flue gas as the self-circulating fluidization medium in the gasifier. The innovations of this paper are mainly as follows: (i) a novel MP-PIC model that considers gas–solid hydrodynamics, heat and mass transfer, and complex chemical reactions, was developed to simulate a dual circulating fluidized bed system for the graded conversion of coal; (ii) the proposed model has been well validated with the experimental measurements under various operating conditions; (iii) the influences of operating parameters and structural parameters on the gas–solid flow and thermochemical characteristics have been comprehensively investigated. The research in this paper is expected to provide a fundamental understanding on the operation optimization, reactor design and scale-up of dual circulating fluidized bed coal graded conversion systems.

The paper is structured as follows: Section 2 details the mathematical model and numerical setup. Section 3 compares the results of numerical simulations of complex turbulent multiphase reactive flows with the experimental results to verify the model's accuracy. Section 4.1 presents the evolution of the gas–solid flow regime in the gasifier and combustor. Section 4.2 explores the distribution of particles and gas components in the gasifier and examines the effects of gasifier operating temperatures and bed material particle size distributions. Section 4.3 investigates the effects of the structural parameters of the gasifier. Conclusions are given in Section 5.

2. Mathematical method

2.1. Governing equations of gas and solid phases

This study developed an MP-PIC model that comprehensively considers gas–solid flow, heat and mass transfer, and chemical reactions. Particles with the same properties are packed by introducing the concept of computational parcel. The reactants and bed material particles are assumed to be spherical due to the limitation of handling non-spherical particles. The gas phase motion in the MP-PIC method is described by the Navier-Stokes equation, while the motion of the particle phase is solved using the particle distribution function (PDF). The governing equations for the gas phase are as follows:

$$\frac{\partial(\alpha_g\rho_g)}{\partial t}+\nabla\cdot(\alpha_g\rho_g\mathbf{u}_g)=\delta\dot{m}_s \tag{1}$$

$$\frac{\partial(\alpha_g\rho_g\mathbf{u}_g)}{\partial t}+\nabla\cdot(\alpha_g\rho_g\mathbf{u}_g\mathbf{u}_g)=-\alpha_g\nabla p+\mathbf{F}+\alpha_g\rho_g\mathbf{g}+\nabla\cdot(\alpha_g\tau_g) \tag{2}$$

$$\frac{\partial(\alpha_g\rho_g h_g)}{\partial t}+\nabla\cdot(\alpha_g\rho_g h_g\mathbf{u}_g)=\alpha_g\left(\frac{\partial p}{\partial t}+\mathbf{u}_g\cdot\nabla p\right)+\varphi-\nabla\cdot(\alpha_g q)+\dot{Q}+S_\mathrm{h}+\dot{q}_\mathrm{D} \tag{3}$$

$$\frac{\partial(\alpha_g\rho_g Y_{gi})}{\partial t}+\nabla\cdot(\alpha_g\rho_g Y_{gi}\mathbf{u}_g)=\nabla\cdot(\rho_g D_g\alpha_g\nabla Y_{gi})+\delta\dot{m}_{i,chem} \tag{4}$$

where $\mathbf{u}_\mathrm{g}$, α_g, and ρ_g are the velocity, volume fraction, and density of the gas phase, respectively. $\delta\dot{m}_\mathrm{s}$ is the change in gas mass per unit volume for heterogeneous gas–solid reactions. p is the pressure, τ_g is the gas stress tensor, and $\mathbf{g}$ is the gravitational acceleration. $\mathbf{F}$ is the interphase momentum exchange phase. h_g is the enthalpy of the gas. φ is the viscous dissipation, $\dot{Q}$ is the energy source per unit volume, and S_h denotes the energy exchange from the particulate phase to the gas phase. Y_{gi} is the mass fraction of species i. $\delta\dot{m}_{i,chem}$ is the chemical source term in the individual gas component transport equation, and D_g is the turbulent mass diffusion coefficient.

The dynamics of the particle phase in the MP-PIC method are determined by solving the PDF (f). The transport equation for f is given as:

$$\frac{\partial f}{\partial t}+\frac{\partial(f\mathbf{u}_s)}{\partial x}+\frac{\partial(f\mathbf{A})}{\partial\mathbf{u}_s}=\frac{f_D-f}{\tau_D}+\frac{f_G-f}{\tau_G} \tag{5}$$

where f_D is the particle distribution function at local equilibrium and τ_D is the particle collision relaxation time. After the particle collision, the velocity tends to an isotropic Gaussian distribution, and f_G and τ_G are the particle distribution function and relaxation time in this state, respectively. The particle acceleration $\mathbf{A}$ is calculated as:

$$\mathbf{A}=\frac{d\mathbf{u}_s}{dt}=D_s(\mathbf{u}_g-\mathbf{u}_s)-\frac{1}{\rho_s}\nabla p-\frac{1}{\alpha_s\rho_s}\nabla\boldsymbol{\tau}_s+\mathbf{g}+\mathbf{F}_s \tag{6}$$

where $\mathbf{u}_\mathrm{s}$, ρ_s, and α_s are the velocity, the density, and the volume fraction of the solid phase, respectively. τ_s is the particle collision stress, $\mathbf{F}_\mathrm{s}$ is the inter-particle friction, and D_s is the drag force coefficient. In the MP-PIC method, the particle phase pressure gradient force is used to characterize the particle collision, and its value increases monotonically with the particle volume fraction [43]. The corresponding force τ_s, corresponding to the particle law, can be solved using the Harris and Crighton model [44]:

$$\tau_s=\frac{P_s\alpha_s}{\max\left[(\alpha_{cp}-\alpha_s),\delta(1-\alpha_s)\right]} \tag{7}$$

where α_cp is the maximum packing density and P_s is a constant with pressure units.

The particle volume fraction α_s, the interphase momentum exchange term $\boldsymbol{F}$, and the interphase energy exchange term S_h are:

$$\alpha_s=\iiint f\frac{m_s}{\rho_s}dm_s d\mathbf{u}_s dT_s \tag{8}$$

$$\mathbf{F}=-\iiint f\left\{m_s\left[D_s(\mathbf{u}_g-\mathbf{u}_s)-\frac{\nabla p_g}{\rho_s}\right]+\mathbf{u}_s\frac{dm_s}{dt}\right\}dm_s d\mathbf{u}_s dT_s \tag{9}$$

$$S_h=\iiint f\left\{m_s\left[D_s(\mathbf{u}_g-\mathbf{u}_s)^2-C_V\frac{dT_s}{dt}\right]-\frac{dm_s}{dt}\left[E_s+\frac{1}{2}(\mathbf{u}_g-\mathbf{u}_s)^2\right]\right\}dm_s d\mathbf{u}_s dT_s \tag{10}$$

where m_s is the particle phase mass and T_s is the particle phase temperature.

In the current model, the temperature distribution inside the particle is assumed to be uniform and the conductive heat transfer from collisions is ignored. The energy exchanged outside the particle consists of the convective heat transfer term Q_sg, the radiative heat transfer term Q_radi, and the chemical reaction heat term Q_react. The energy conservation equation for the particle phase is [45]:

$$m_s C_V\frac{dT_s}{dt}=Q_{sg}+Q_{radi}+Q_{react} \tag{11}$$

$$Q_{sg}=\frac{\kappa_g\mathrm{Nu}_s}{d_s}A_s(T_g-T_s) \tag{12}$$

$$Q_{radi}=\sigma\varepsilon_s A_s(T_{s,local}^4-T_s^4) \tag{13}$$

$$\mathrm{Nu}_s=2.0+0.6\mathrm{Re}_s^{1/2}Pr^{1/3} \tag{14}$$

$$\mathrm{Re}_s=\frac{\rho_g\varepsilon_g|\mathbf{u}_g-\mathbf{u}_s|d_s}{\mu_g} \tag{15}$$

$$\mathrm{Pr}=\mu_g C_{s,g}/\kappa_g \tag{16}$$

2.2. Inter-phase drag correlations

The calculation of drag force F_p relates to the fluid conditions, the drag coefficient, and the Reynolds number between the gas and the particles. It can be calculated by [46]:

$$F_p=m_s C_d|\mathbf{u}_f-\mathbf{u}_s| \tag{17}$$

where C_d represents the drag coefficient between the gas and the particle.

So far, many models have been proposed to calculate the drag force. The EMMS-Yang drag model proposed by Yang et al [47] and Li et al [48] is used in this study, which considers the effect of mesoscale flow structures such as particle clusters as well as bubbles on the flow. The constants in the model are adopted from the experimental results. The calculation formula is as follows:

$$D_s = \frac{9}{2}\frac{\mu_f}{\rho_p r_p^2} f_e \tag{18}$$

$$f_e = \begin{cases} \frac{1}{18\theta_f}\left(150\frac{\theta_p}{\theta_f} + 1.75\mathrm{Re}\right) & \theta_f < 0.74 \\ \left(1 + 0.15\mathrm{Re}^{0.687}\right)\omega & \theta_f \geqslant 0.74 \quad and \quad \mathrm{Re} < 1000 \\ 0.44\frac{\mathrm{Re}}{24}\omega & \theta_f \geqslant 0.74 \quad and \quad \mathrm{Re} \geqslant 1000 \end{cases} \tag{19}$$

$$\omega_e = \begin{cases} -0.576 + \frac{0.0214}{4\left(\theta_f + 0.7463\right)^2 + 0.0044} & 0.74 \leqslant \theta_f < 0.82 \\ -0.0101 + \frac{0.0038}{4\left(\theta_f + 0.7789\right)^2 + 0.004} & 0.82 < \theta_f \leqslant 0.97 \\ -31.8295 + 32.8295\theta_f & 0.97 < \theta_f \leqslant 1 \end{cases} \tag{20}$$

2.3. Chemical reactions

Upon entering the gasifier, coal particles are subjected to rapid pyrolysis under high temperatures. This process leads to the fast precipitation of volatile components in the coal powder, while the remaining coke undergoes conversion with the gas introduced into the reactor. As the reaction progresses over a certain time, incompletely reacted coke becomes enveloped by the particle flow and subsequently burned in the combustor. The high-temperature gas produced by coal pyrolysis is purified and cooled by ash removal at the outlet of the gasifier's cyclone separator, and most of it is sent back to the gasifier as a fluidization medium. The coal utilized in this study comes from a test coal sample provided by Shanxi GEM International Energy Co. Ltd. The industrial and elemental analyses of the coal particles are detailed in Table 1.

In this work, the coal pyrolysis process is described as follows:

$$\mathrm{Coal} \rightarrow \alpha_1\mathrm{CO} + \alpha_2\mathrm{CO_2} + \alpha_3\mathrm{CH_4} + \alpha_4\mathrm{H_2} + \alpha_5\mathrm{H_2O} + \alpha_6\mathrm{Tar} + \alpha_7\mathrm{H_2S} + \alpha_8\mathrm{NH_3} + \alpha_9\mathrm{C_2H_6}, \sum_i \alpha_i = 1 \tag{R1}$$

where the coefficients of the products in the equations are calculated based on the proximate analysis and ultimate analyses of the coal particles.

The pyrolysis process is described by a single-step one-stage Areneus reaction rate:

$$\frac{dm_{\mathrm{volatile}}}{dt} = c_0\exp\left(-\frac{E}{T}\right)m_{\mathrm{volatile}} \tag{21}$$

where m_{volatile} is the mass of volatile components in the coal particles and T is the particle temperature. After pyrolysis, the char remaining in the coal particles reacts with H_2O, CO_2, and H_2 to form CO, H_2, and CH_4. In addition to heterogeneous reactions associated with char gasification, homogeneous reactions are also considered in the reactor such as water gas shift reaction and methane gasification reaction. There are thousands of homogeneous and heterogeneous chemical reactions in the practical CFB reactor with coal pyrolysis, gasification, and combustion. For the sake of simplification, it is necessary to make an assumption that the primary conversion of gas and solid species in the reactor can be characterized by a set of 14 chemical reactions given in Table 2.

Table 2
Chemical reaction and reaction rates [9,49–54].

Chemical reaction equation	Kinetic parameters
$\mathrm{R2: H_2O(s) \rightarrow H_2O(g)}$	$r_2 = 5.13 \times 10^4\exp(-15585/T)m_{\mathrm{H_2O}}$
$\mathrm{R3: C + H_2O \rightarrow CO + H_2}$	$r_3 = 6630T\exp(-13645/T)m_{\mathrm{C}}[\mathrm{H_2O}]$
$\mathrm{R4: C + CO_2 \rightarrow 2CO}$	$r_4 = 0.636T\exp(-31624/T)m_{\mathrm{C}}[\mathrm{CO_2}]$
$\mathrm{R5: C + 2H_2 \rightarrow CH_4}$	$r_5 = 2.838 \times 10^8 T\exp(-15078/T - 7.087)m_{\mathrm{C}}[\mathrm{H_2}]$
$\mathrm{R6: Tar \rightarrow 7.75C_2H_6 + 0.18CO + 2.86CH_4}$	$r_6 = 288850\exp(-8804.2/T)[\mathrm{Tar}]$
$\mathrm{R7: CO + H_2O \rightarrow CO_2 + H_2}$	$r_7 = 90680\exp(-10640/T)[\mathrm{CO}]^{0.5}[\mathrm{H_2O}]$
$\mathrm{R8: CO_2 + H_2 \rightarrow CO + H_2O}$	$r_8 = 640\exp(-43260/T)[\mathrm{H_2}]^{0.5}[\mathrm{CO_2}]$
$\mathrm{R9: CH_4 + H_2O \rightarrow CO + 3H_2}$	$r_9 = 2.85 \times 10^{-3}\exp(-45042/T)[\mathrm{H_2O}][\mathrm{CH_4}]$
$\mathrm{R10: C + O_2 \rightarrow CO_2}$	$r_{10} = 6.34\exp(-22590/T)m_{\mathrm{C}}[\mathrm{O_2}]$
$\mathrm{R11: CO + 0.5O_2 \rightarrow CO_2}$	$r_{11} = 7.63 \times 10^6 T\exp(-13155/T)[\mathrm{CO}][\mathrm{O_2}]^{0.5}$
$\mathrm{R12: H_2 + 0.5O_2 \rightarrow H_2O}$	$r_{12} = 6.2 \times 10^6 T\exp(-10110/T)[\mathrm{H_2}][\mathrm{O_2}]$
$\mathrm{R13: CH_4 + 2O_2 \rightarrow CO_2 + 2H_2O}$	$r_{13} = 3.51 \times 10^{-5}T\exp(-48417/T)[\mathrm{CH_4}]^{0.7}[\mathrm{O_2}]^{0.8}$
$\mathrm{R14: C_2H_6 + 3.5O_2 \rightarrow 2CO_2 + 3H_2O}$	$r_{14} = 3.51 \times 10^5\exp(-16417/T)$

3. Simulation setting and model validation

3.1. Numerical settings

The CFB system investigated in this study is a 1 MWth circulating fluidized bed staged conversion cogeneration system developed by the Institute of Thermal Engineering at Zhejiang University. Due to its complex structure and operating conditions, the current work simplifies the system without considering auxiliary components such as the dust collector, scrubber tower, and gas intercooler. Fig. 1 represents the simplified geometry configuration, which includes a combustor, gasifier, loop seals, and cyclone separators.

The coal particles used in the current work are 1200 kg/m^3 in density and the particle size distribution is detailed given in Table 3. In this study, coal particles are assumed to be solid spherical particles. The density of the coal particles changes with the chemical reaction, and the particle size and shape remain unchanged. The sand is used as the bed material with a density of 2500 kg/m^3 and the particle size is adopted as a wide sieve ranging from 100 μm to 200 μm. The initial solid holdup is set to 0.22 for the gasifier and 0.3 for the combustor.

In the gasifier and combustor, sand particles are initially packed at the bottom, and coal particles are packed in the combustor. At the start time, the bed height is 3.7 m for the gasifier and 6.64 m for the combustor. The entire system is initially filled with air and the operating temperatures in the gasifier and combustor are 873 K and 1083 K, respectively. Coal particles are introduced into the gasifier from the side, while the purified syngas are fed in from the bottom. To monitor the composition of the output product gas, a monitoring surface is set at the outlet of the gasifier's separator. Air is introduced from the bottom of the combustor, with four secondary air streams symmetrically introduced from its bottom. Steam is utilized for pellet fluidization at the loop seal. The boundary conditions are defined as mass flow inlet, with an outlet pressure set at 101325 Pa. The normal-to-wall momentum retention coefficient and tangent-to-wall momentum retention coefficient are both set to 0.9. The computational time step employed is 5 × 10^{-4} s. Detailed operating parameters can be found in Table 4.

Table 1
Proximate analysis and Ultimate analysis of coal.

Proximate analysis (%)					Calorific value		Ultimate analysis (%)				
M_{ad}	M_{ar}	A_{ad}	V_{ad}	FC_{ad}	$Q_{net,ar}$ kJ/kg	$Q_{net,ar}$ kcal/kg	C_{ad}	H_{ad}	N_{ad}	$S_{t,ad}$	O_{ad}
0.86	6.58	41.96	27.80	29.38	14,118	3376	41.07	2.97	0.69	1.65	10.80

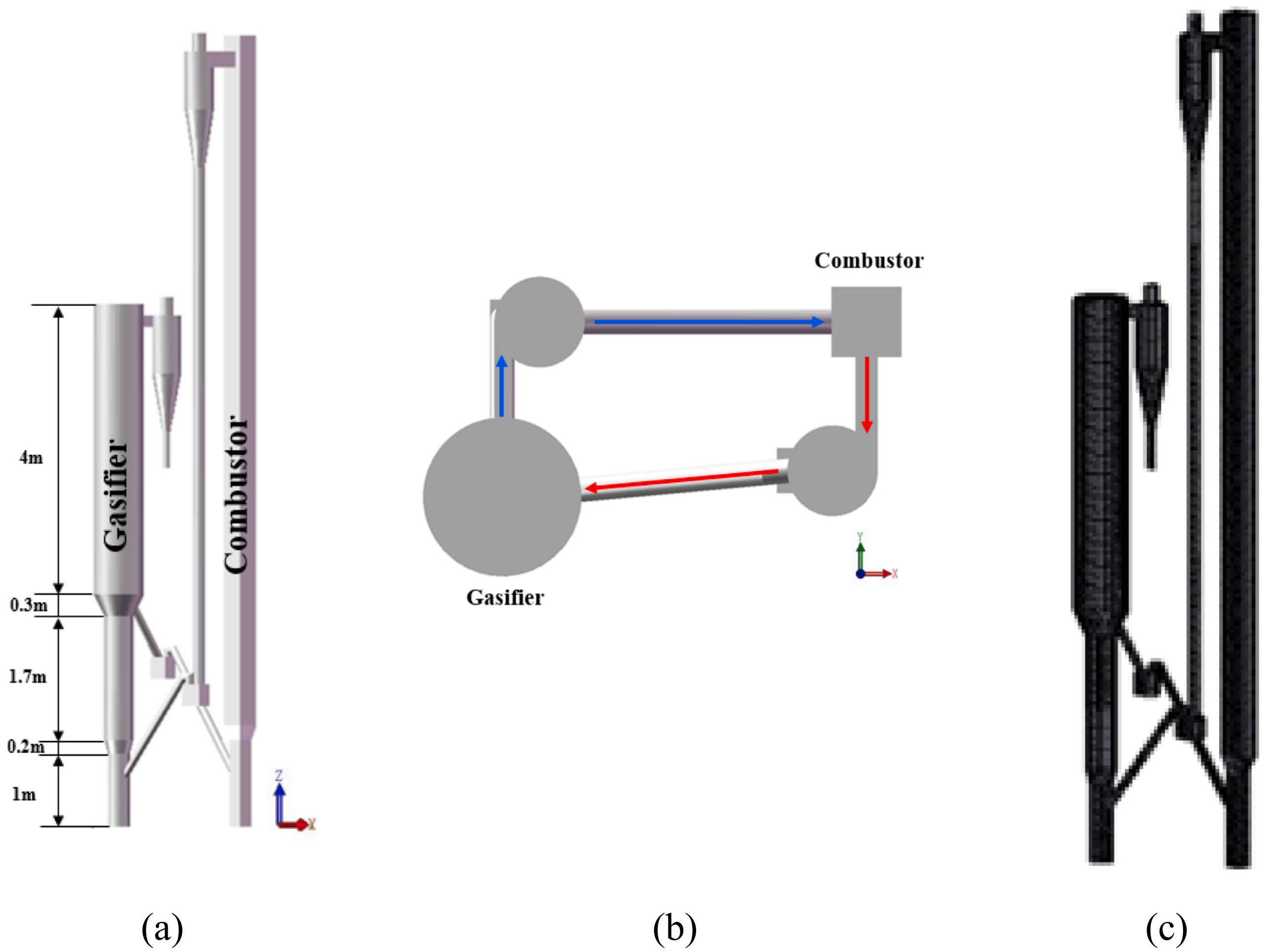

Fig. 1. Schematic of geometry configuration: (a) front view and dimensions; (b) top view; (c) grids.

Table 3
Particle size distribution of coal.

Particle diameter	Percentage(%)
< 0.45 mm	44.73
0.45–0.9 mm	20.73
0.9–1.25 mm	0.96
1.25–2.5 mm	20.13
2.5–4.0 mm	7.10
4.0–6.0 mm	5.68
6.0–8.0 mm	0.67

Table 4
Details of Operational parameters.

Parameters	Value
Coal feed rate (kg/h)	201.6
Coal particle temperature (K)	300
Gasifier gas flow rate (kg/h)	201.6
Gsifer gas temperature (K)	473
Combustor inlet air velocity (m/s)	2
Combustor inlet air temperature (K)	383
Loop seal steam velocity (m/s)	0.2
Loop seal steam temperature (K)	400
Total secondary air flow rate (kg/h)	162
Secondary air temperature (K)	600

3.2. Sensitivity analysis

The selection of the number of grids can significantly impact the accuracy of simulation results. Therefore, to evaluate this effect, grid-independence analysis is performed before simulation. The computational domain is divided into three sets of grids with different

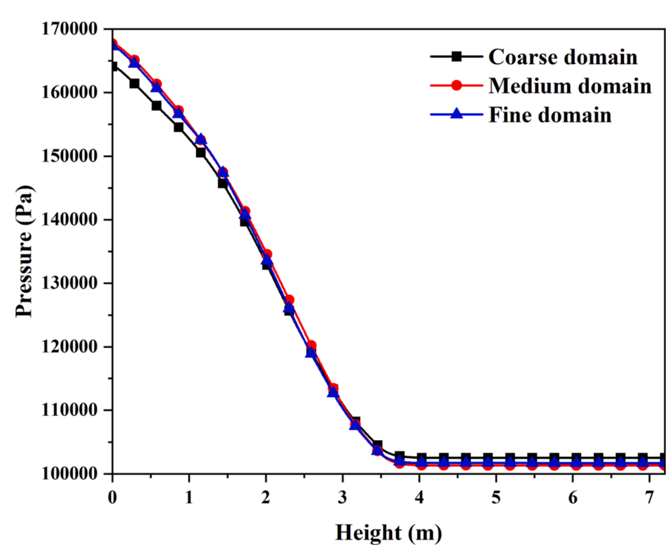

Fig. 2. Time-averaged axial distribution of pressure under different resolutions.

resolutions, i.e., fine (390392), medium (240240), and coarse grids (190944). The time-averaged axial distribution of pressure in the gasifier is monitored and compared, as shown in Fig. 2 The results indicate that the pressure decreases with the increase in height and stabilizes at a fixed value. The axial pressure distribution obtained from the simulations using fine and medium grids is generally consistent, while the results using the coarse grid show great differences. Therefore, to balance the accuracy and efficiency of the calculation, the medium grids are suitable for the subsequent simulations.

The selection of the statistical time in post-processing can also impact the final calculation results. Fig. 3(a) illustrates that the mass fraction of each gas component reaches dynamic stability after 80 s. Therefore, the time-averaged mole fractions of each exit gas component are statistically calculated for three time periods: 80–85 s, 80–100 s, and 80–150 s, as presented in Fig. 3(b). Notably, the time-averaged mole fractions of each exit gas component are nearly identical across these three statistical periods. Consequently, the subsequent analysis in this work will focus on the data from the 80–85 s period to reduce the calculation time.

3.3. Model validation

To validate the accuracy of the developed model, Fig. 4 illustrates the numerical simulation results of the normalized time-averaged mole fraction of each gas component at the outlet of the cyclone separator of the gasifier in comparison with the experimental data. The predictions for CH_4 and H_2 are within 5 % of the experimental data, and for CO_2, CO, and C_2H_6 within 20 %. These discrepancies may be caused by the simplification of intricate homogeneous and non-homogeneous reactions that occur during the practical staged conversion of coal. Considering these complete chemical reactions are impractical, the model employs simplified empirical parameters for global reactions and reaction kinetics. Additionally, different literature provides different values for reaction kinetics. Consequently, disparities between the simulation results and experimental results in an industrial-scale fluidized bed are inevitable but acceptable. Fig. S1 of the supporting information shows the simulation results, experimental results, and relative errors of the normalized time-averaged mole fraction of the gas components at the outlet of the gasifier's cyclone separator with different operating temperatures. It can be seen that the trend of the gas component content change with temperature is consistent with the engineering reality. The simulation results at all temperatures are in better agreement with the experimental results. Overall, the current model is reliable in predicting the hydrodynamics and thermochemical behavior of a CFB coal staged conversion cogeneration system.

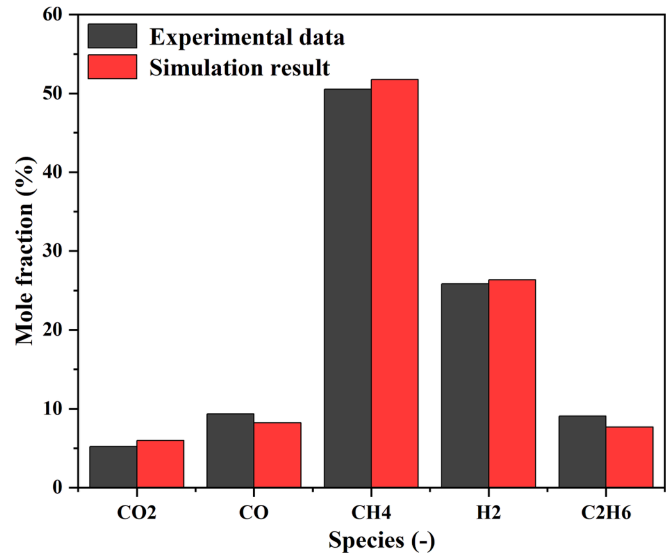

Fig. 4. Comparison of simulation results and experimental data for the time-averaged mole fractions of each gas component at the outlet of the gasifier's cyclone separator.

4. Results and discussion

4.1. General flow patterns

In this paper, the modified polydisperse force model is employed to improve the prediction accuracy of gas–solid flow characteristics in the system. Fig. 5 illustrates the time-evolution distribution of particles in the coal staged conversion reactor (colored by the volume fraction of particles). Initially, sand particles accumulate in the gasifier, combustor, and loop seal, while coal particles accumulate in the combustor. As the fluidized gas is introduced from the bottom of the gasifier, the height of

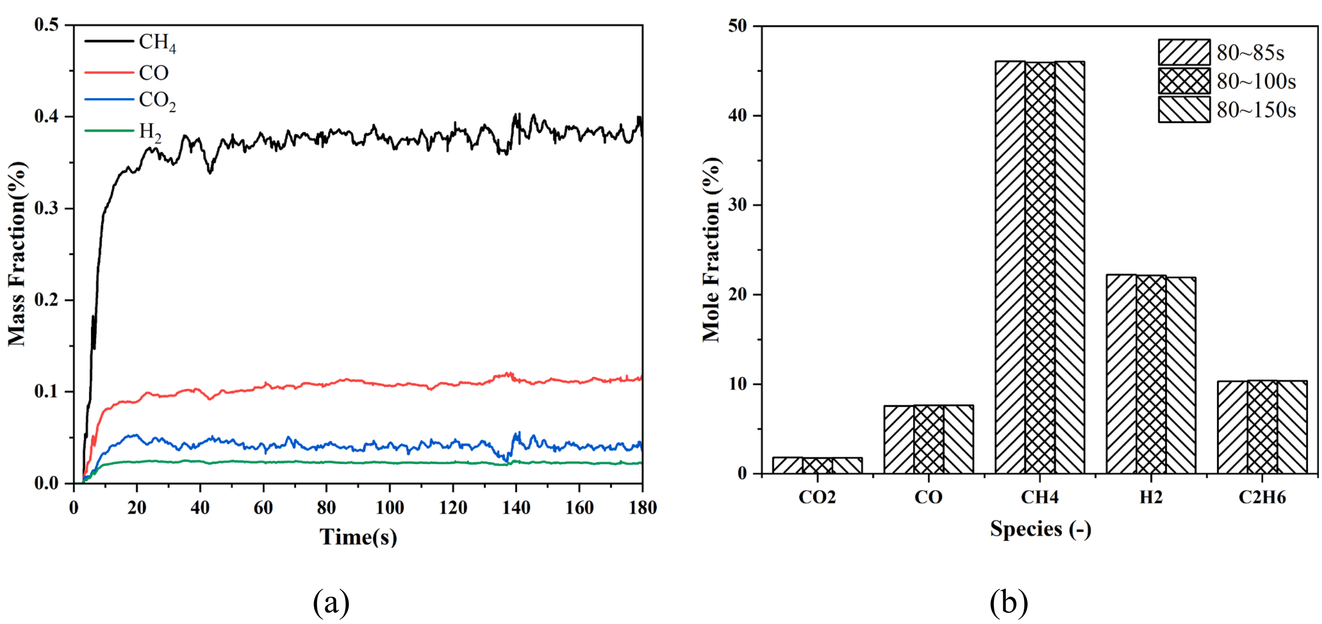

Fig. 3. (a) Time evolutions of gas components at the gasifier outlet; (b) time-averaged mole fractions for different statistical times.

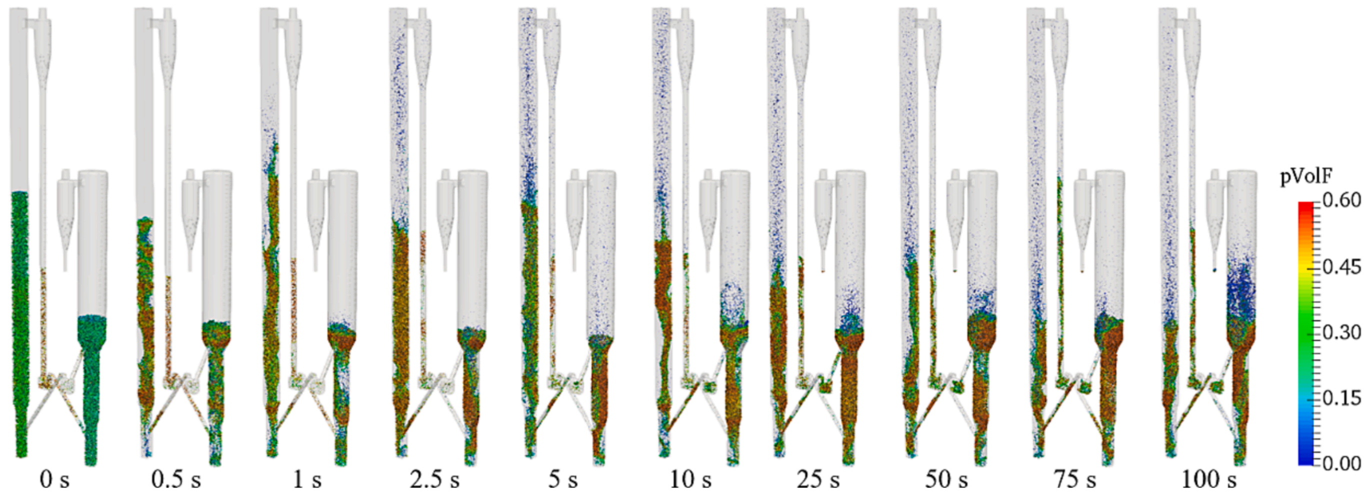

Fig. 5. Time evolution of gas–solid flow patterns in the reactor (colored by the volume fraction of particles).

the bed material substantially increases with the expansion of the mixed particles. Visible bubbles form in the bed particles, gradually increasing in size as they rise until eventually break up at the bed surface. At approximately 2.5 s, particles enter the cyclone separator of the combustor and rotate down along the cyclone wall by gravity and centrifugal force before entering the return circuit. In the gasifier, the volume fraction of the bed material particles is higher in the expanding section of the dense-phase zone and at the bottom of the rare-phase zone. Coal particles are injected from the side at the height of 3.6 m and undergo intense mixing, heat transfer, and chemical reaction with the bed material particles, where the coal pyrolysis reaction predominantly occurs.

4.2. Operating parameters

4.2.1. Gasifier operating temperature

The operating temperature of the gasifier is a crucial parameter for cogeneration system operation. It not only impacts the composition and yield of gas, tar, and semi-coke produced from coal pyrolysis but also influences the operation of the circulating fluidized bed combustor through the generated semi-coke. Thus, three different gasifier operating temperatures (i.e., 600 °C, 650 °C, and 700 °C) are set to investigate its influence on the generation of the main gas components (CH_4, H_2, CO_2, and CO) in the gasifier. Fig. 6 shows the time-averaged temperature distribution of axial gas in the gasifier at different operating temperatures and the mole fraction of gas components at the outlet of the gasifier. In addition, Fig. S2 of the supporting information shows the time-averaged gas mass fraction distribution in the central slice of the gasifier. It shows that the operating temperature of the gasifier has a certain influence on the composition of the gas precipitated and formed during the coal pyrolysis process.

Specifically, as the operating temperature of the gasifier increases, the axial time-averaged temperature distribution increases accordingly, showing approximately 640–670 °C, 680–700 °C, and 710–730 °C, respectively. Furthermore, the axial temperature distribution in the gasifier exhibits a characteristic of lower temperatures at the bottom region and higher temperatures at the top zone. This is attributed to the fact that coal particles entering the gasifier from the bottom absorb a

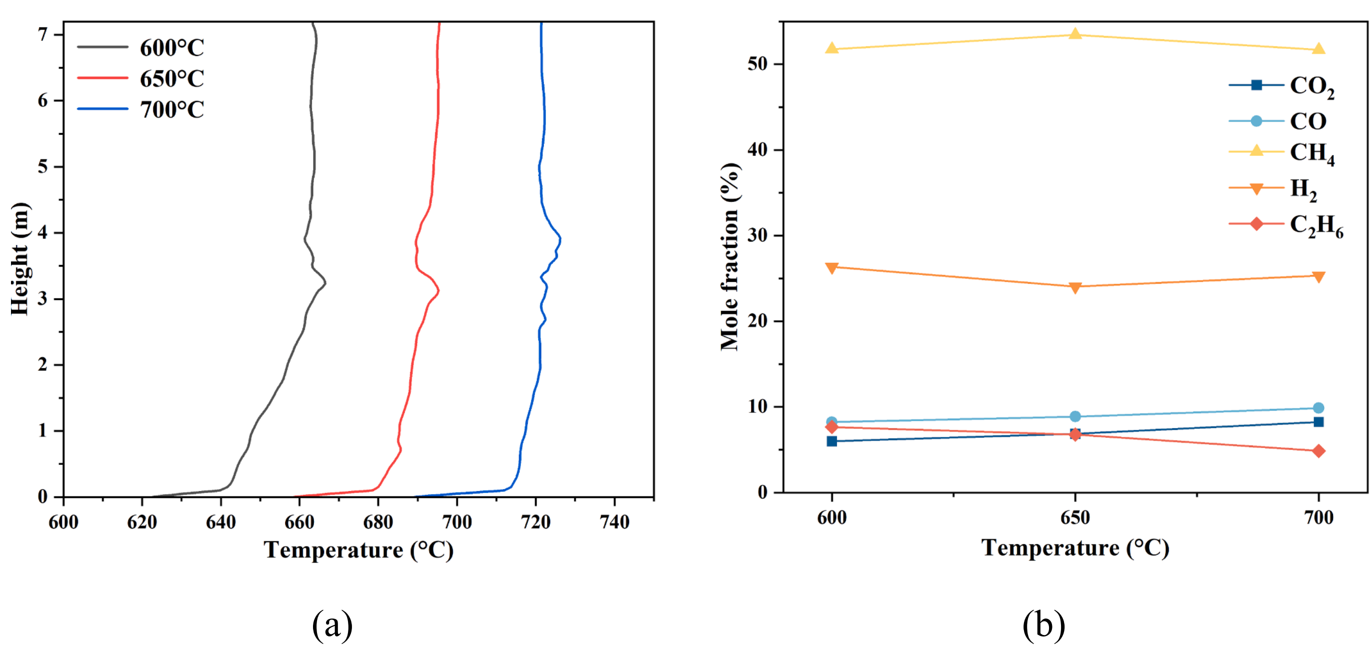

Fig. 6. (a) Distribution of axial time-averaged gas temperature in the gasifier; (b) mole fraction of gas components at the outlet of the gasifier's cyclone separator with different operating temperatures.

substantial amount of heat due to pyrolysis and gasification reactions. However, as the high-temperature sand particles recycle from the combustor into the gasifier, the temperature in the gasifier increases. Additionally, from Fig. 6(a), it can be observed that the upper temperature in the gasifier remains basically constant, indicating that the heat and mass transfer processes in the gasifier have essentially reached dynamic stability. Moreover, the temperature distributions in the gasifier under different operating conditions closely align with the measured results in engineering practice, and the maximum error is less than 20 %. With the increase in temperature, the content of CO and CO_2 in the gas exported from the gasifier increased, which is mainly due to the increase of gasifier temperature promoting the splitting of large molecular chains and the generation of small molecules of gas. C_2H_6 decreases with the increase of gasifier temperature. The content of CH_4 initially increases and then decreases with the increase of gasifier temperature, and the highest mole fraction is about 53 % at 650 °C. The content of H_2 decreases initially and then increases.

Fig. S2 of the supporting information shows that CH_4 and H_2 have a high mass fraction at the bottom of the rare-phase zone. This finding indicates the violent mixing of coal particles with sand particles in this region, which represents the primary site of the pyrolysis reaction. The dense-phase zone has a higher mass fraction of CO and C_2H_6 compared to the rare-phase zone. A distinct low mass fraction region is observed at the exit from the loop seal to the combustor. In this region, some of the bed material from the gasifier is transferred to the combustor, causing a localized decrease in the mass fraction of each gas product.

4.2.2. Particle size distribution (PSD) width

Sand particles are utilized as the bed material in both the gasifier and the combustor. Assuming that the particle shape is spherical, the particle size distribution (PSD) is described by a lognormal distribution, which is defined as:

$$f(d_p) = \frac{1}{d_p \sigma \sqrt{2\pi}} e^{-\frac{(\ln(d_p)-\mu)^2}{2\sigma^2}} \tag{22}$$

where μ is the mean diameter, σ is the standard deviation, and d_p is the particle diameter. To evaluate the impact of PSD on the gasifier's performance, three different PSD widths (σ/μ) for the bed material particles were considered. Fig. 7 shows the particle size distribution of bed material particles with different distribution widths, such as 0.01, 0.03, and 0.05, respectively.

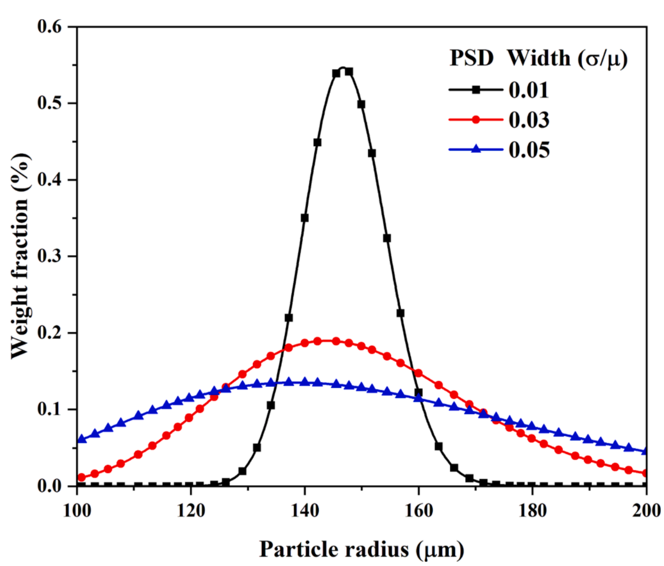

Fig. 7. Particle size distribution of bed material particles with different distribution widths (σ/μ).

In the gasifier, the proportion of bed material particles is far more than that of coal particles. Coal particles undergo mixing and collisions with bed material particles at the bottom of the rare-phase zone. Therefore, the bed material particles play a crucial role in the heat and mass transfer and chemical reaction processes. Fig. 8(a) presents the time-averaged distribution of axial particle volume fraction in the gasifier with different PSD widths. Regardless of PSD width, the axial particle volume fraction distribution exhibits a consistent trend in the gasifier. The high velocity of fluidized gas enables bed material particles of all sizes to be entrained from the dense-phase zone to the rare-phase zone along with the gas. Large-size bed material particles do not accumulate in the lower part of the gasifier. In the lower part, the particle volume fraction increases with height. However, as the particles enter the gasifier at an oblique downward angle, a short decline in particle volume fraction can be observed above the inlet position of the loop seal. Subsequently, the increase of volume fraction can be observed until reaching a peak in the enlarged section of the dense-phase zone. In the tapering section between the dense-phase zone and the rare-phase zone, another loop seal returns the bed material from the gasifier back to the combustor, resulting in a rapid decrease in particle volume fraction at that height.

Fig. 8(b) displays the time-averaged distribution of particle volume fraction in the central slice of the gasifier under different PSD widths. It can be observed that as the PSD width increases, the particle size distribution becomes more uneven. Air bubbles tend to overflow from the sides of the bed, and the "core-annulus" structure in the enlarged section of the dense-phase zone gradually disappears. When the PSD width equals 0.03, the particle volume fraction is high near the wall of the dense-phase zone and the tapering section, while becomes small in the bottom of the rare-phase zone. This section also exhibits the lowest axial particle volume fraction.

Fig. 9 shows the time-averaged axial distribution of gas component mass fractions in the gasifier with different PSD widths. Purified gas is used as the fluidized gas which is introduced from the bottom of the gasifier, resulting in gentle changes in CH_4 and H_2 mass fractions at the bottom of the dense-phase zone. At approximately 0.8 m, minor fluctuations can be observed due to loop seal gas flow perturbations and stabilize afterward. A rapid reduction in the mass fractions of CH_4 and H_2 occurs as the gasifier transitions from the expanding section of the dense-phase zone to the tapering section of the rare-phase zone due to the swift change in inner diameter. Subsequently, coal particles undergo pyrolysis in the gasifier, which causes a rapid increase of CH_4 and H_2 mass fractions until they reach a stable value in the upper part of the rare-phase region. The comparison results show that when the PSD width (σ/μ) equals 0.03, the mass fraction of CH_4 at the gasifier's outlet is lower than in cases with smaller and larger PSD widths, whereas the H_2 content is higher. Furthermore, the purified gas introduced into the gasifier contains a minimal amount of O_2, leading to the conversion of CO to CO_2 at the dense-phase zone and consequent changes in mass fraction. The mass fraction of CO is lower at the top of the rare-phase zone for medium PSD widths than in the cases with smaller and larger PSD widths. When the PSD width (σ/μ) equals 0.05, the mass fractions of CO and CO_2 at the top outlet of the rare-phase zone are the highest.

4.3. Structural parameters

The structural parameters of the reactor have a significant impact on the material distribution, facade arrangement, and overall project cost. Consequently, this section investigates the effects of dense-phase zone enlarged section diameter, rare-phase zone height, and diameter on particle mixing within the bed. The result can provide a theoretical basis and data support for pyrolysis industrial plant structural optimization.

4.3.1. Diameter of the expanding section of the dense-phase zone

Initially, the bed material is piled up to the bottom of the rare-phase zone, and the coal particles are fed in from the bottom of the rare-phase

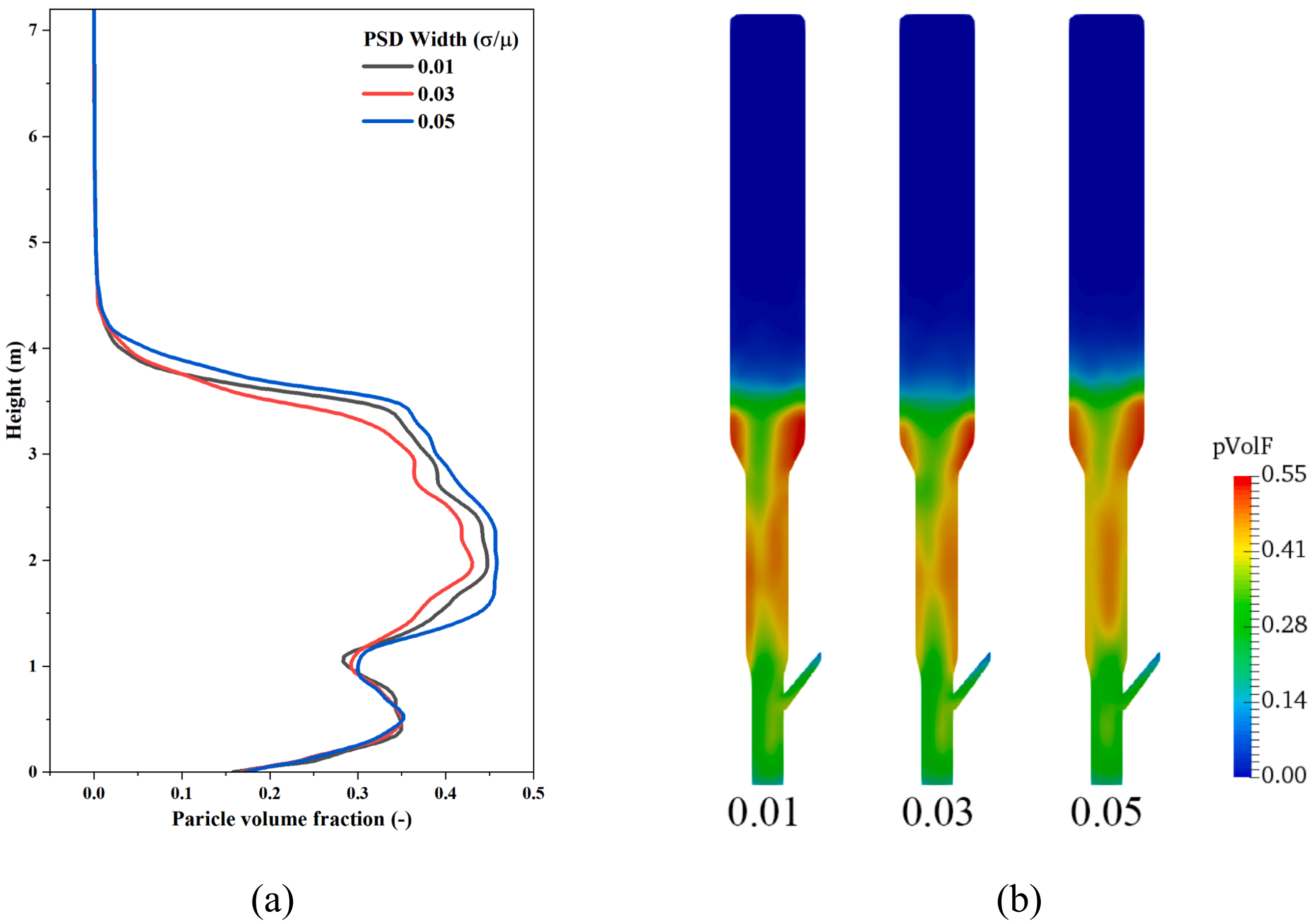

Fig. 8. Time-averaged particle volume fraction distributions of the gasifier at different PSD widths: (a) axially, (b) in the central slice.

zone. Thus, the fluidization state of the dense-phase zone significantly affects the pyrolysis process of biomass particles. The expanding section in the dense-phase zone has a higher particle volume fraction under the influence of the loop seal and fluidizing wind than at the bottom. To investigate the effects of the dense-phase zone's expanding section diameter, three sets of gasifier structures are designed with diameters of 0.35 m, 0.45 m, and 0.50 m, while the dense-phase zone diameter is still 0.40 m. The numerical studies are conducted under identical operating conditions.

Fig. 10 displays the radial time-averaged particle volume fraction and z-direction particle velocity distributions at varying heights within the gasifier, where H is the initial bed height of the gasifier. Fig. 11 shows the time-averaged particle volume fraction distribution in the central slice of the gasifier. Due to the intensive mixing and collision process of particles, the particle volume fraction and axial velocity are asymmetric and show complex radial distributions. At the lower region of the gasifier, the particle volume fraction is higher in the center and lower near the wall because of the unilateral material return from the loop seal. With the increase in height, the particle volume fraction gradually displays a low-in-the-middle, high-near-the-wall radial phenomenon due to wall effects. Within the dense-phase zone's expanding and rare-phase zones ($h/H = 0.5, 0.7, 0.9$), the middle particle content decreases with height. Near the bottom of the rare-phase zone, particle accumulation can be observed near the wall due to the tapering section and loop seal.

Fig. 11 demonstrates that the rare-phase zone partially evolves into gradually homogeneous radial solidity distribution as the axial height increases. The axial velocity of the particles displays an inverse trend compared to the particle volume fraction. As the height increases, the axial velocity transitions from low in the middle of the bottom and high near the wall to high in the middle and low near the wall. This illustrates the presence of a "core-annulus" flow structure in the upper and middle parts of the reactor. Increasing the diameter of the expanding section of the dense-phase zone leads to the appearance of a "core-annulus" structure at a lower position in the gasifier, resulting in a decrease in particle volume fraction at the tapering section and the bottom of the rare-phase zone. This indicates that increasing the diameter of the expanding section can improve the fluidization state. However, as the diameter of the expanding section increases, a gradual decrease can be observed in bed material particles at the bottom of the rare-phase zone. This is because the existence of the tapering section makes part of the bed material particles stay in the rare-phase zone for a long time. Moreover, an internal reflux flow is formed in the tapering section and the bottom of the rare-phase zone, which impedes particles along the wall in the expanding section of the dense-phase zone to enter the tapering section. Furthermore, increasing the diameter of the expanding section of the dense-phase zone results in a lower gas velocity in this region. Consequently, the internal reflux effect at the tapering section is weakened, leading to a decrease in particle volume fraction in this region. Since coal particles need to be mixed with sand particles at the bottom of the rare-phase zone to absorb heat, the reduction of bed material particles in this region also affects the pyrolysis reaction of coal in the gasifier.

Fig. S3 of the supporting information shows the time-averaged mass fraction distribution of gas components in the central slice of the gasifier. It reveals that the reaction area for coal pyrolysis expands upward due to the decrease in particle volume fraction at the bottom of the rare-phase zone. As a result, the mass fractions of CH_4, H_2, and CO at the

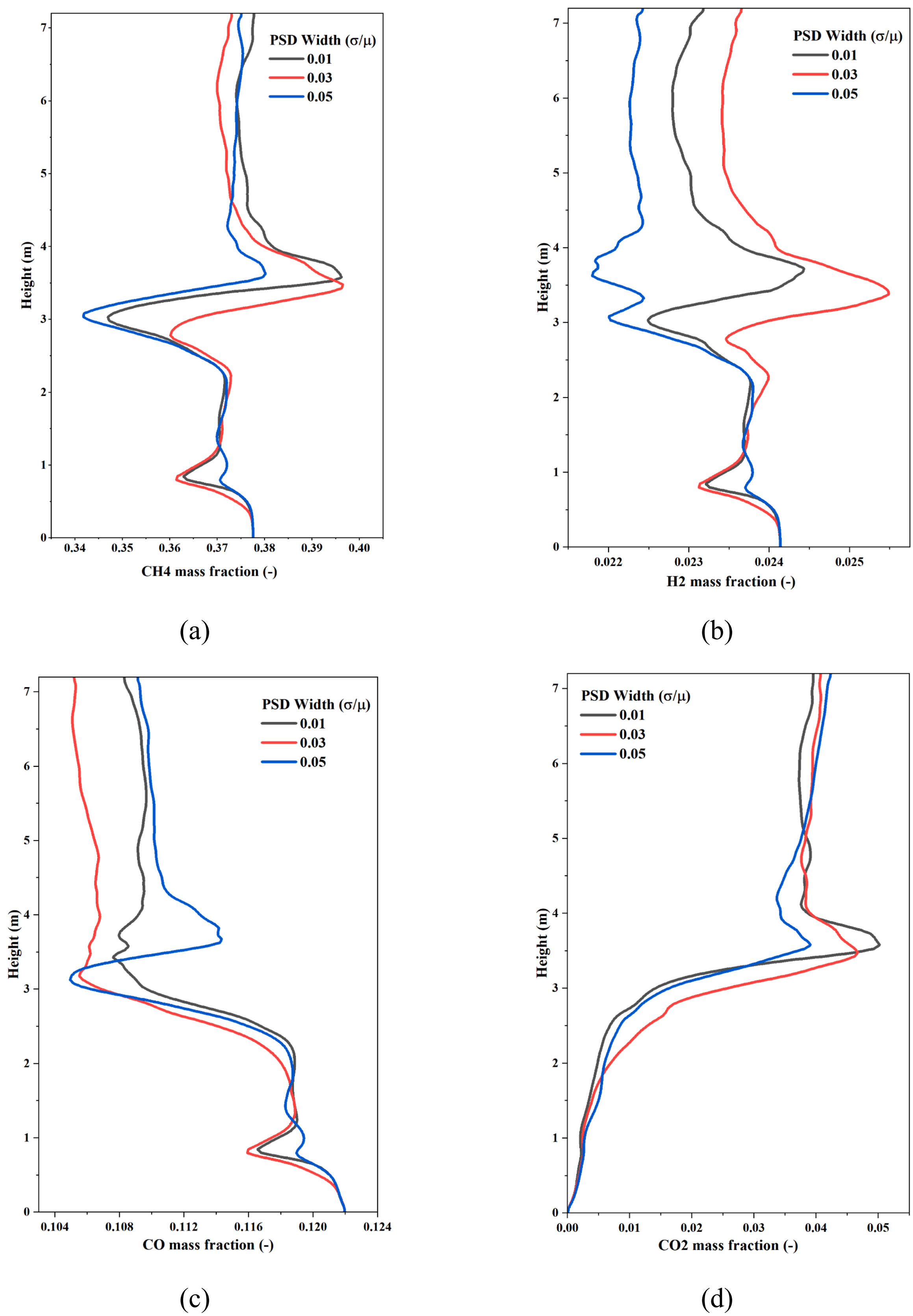

Fig. 9. Time-averaged distribution of gas components mass fraction in the gasifier axial direction for different PSD widths: (a) CH_4; (b) H_2; (c) CO; (d) CO_2.

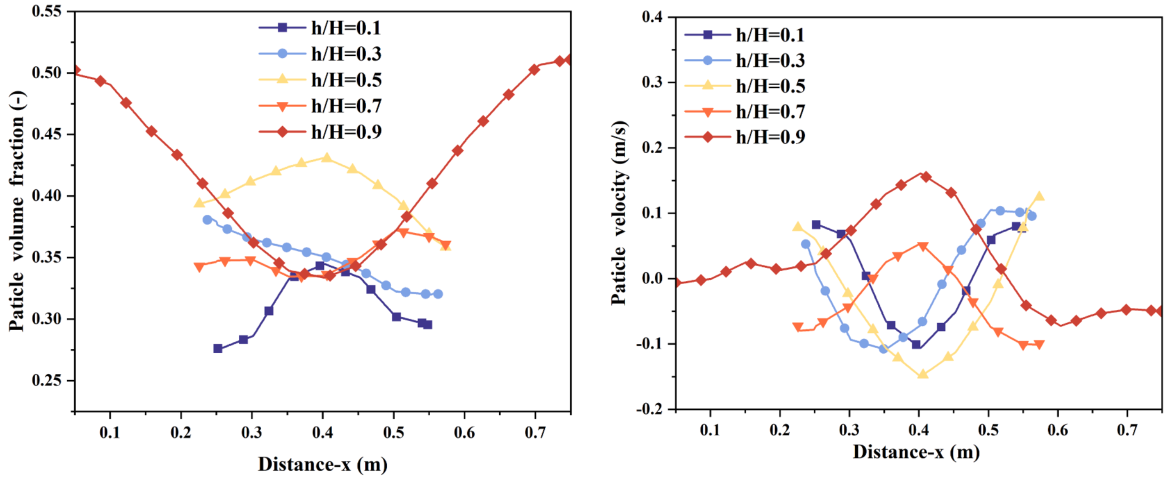

(a)

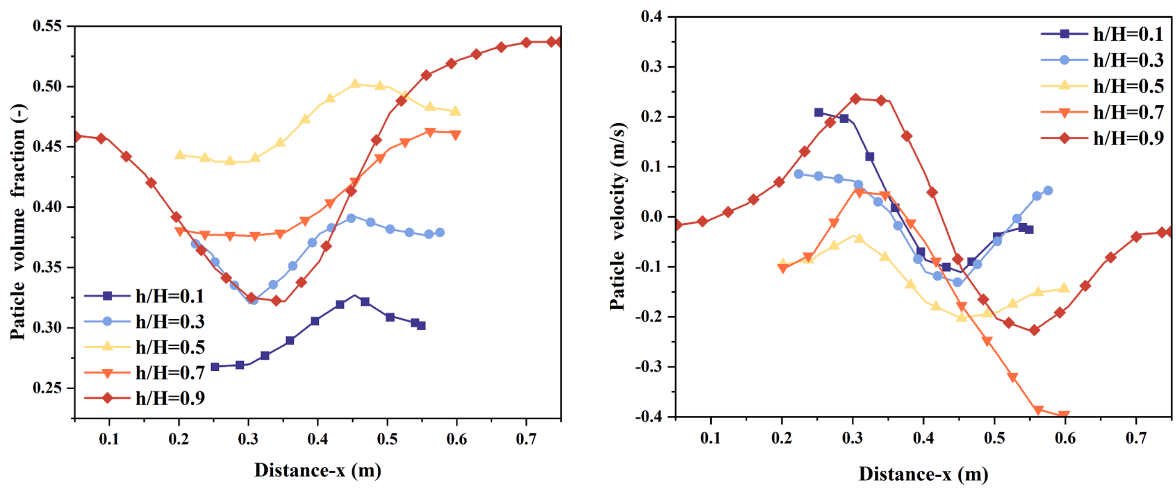

(b)

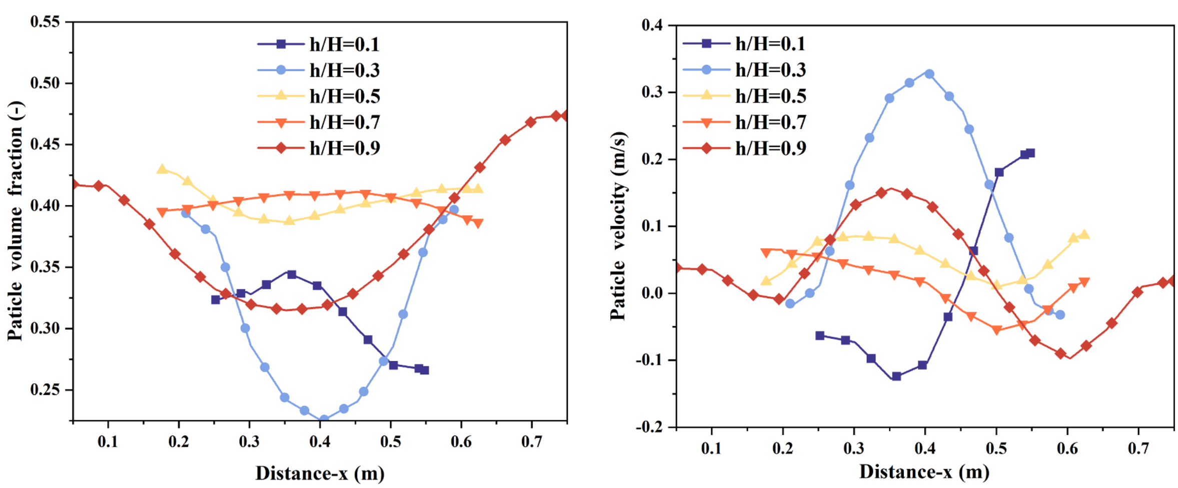

(c)

Fig. 10. Radial time-averaged particle volume fraction and z-direction particle velocity distributions at different heights within the gasifier with different diameters of the dense-phase zone's enlarged section: (a) 0.35 m; (b) 0.40 m; (c) 0.45 m; (d) 0.50 m.

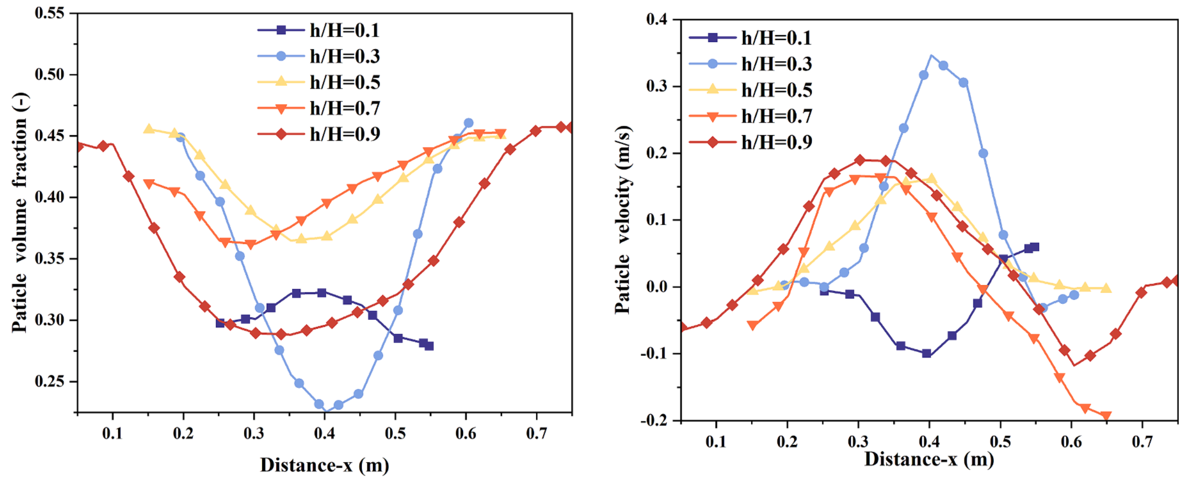

(d)

Fig. 10. (*continued*).

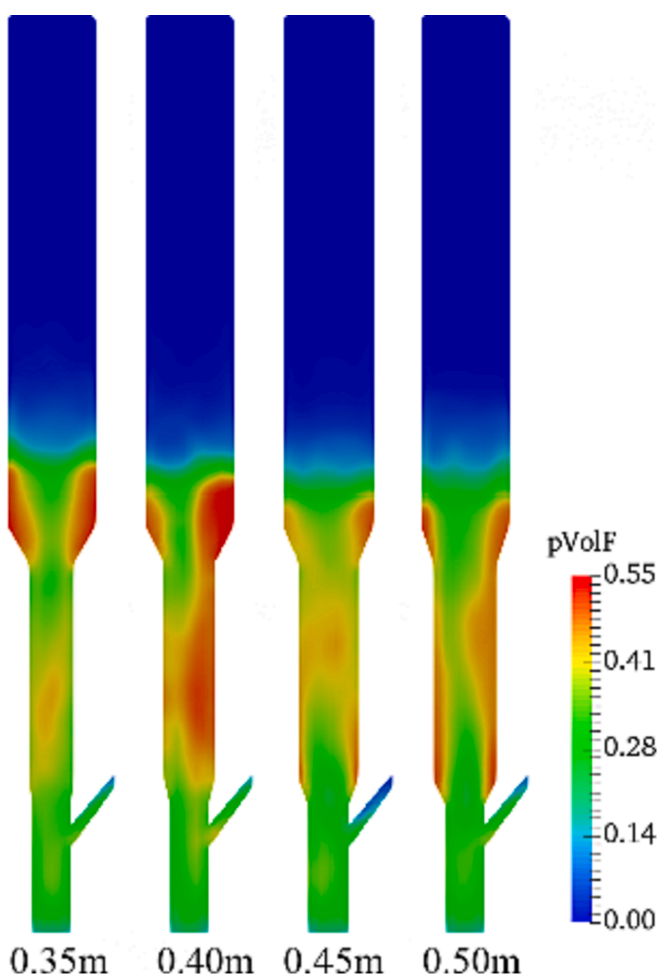

Fig. 11. Time-averaged particle volume fraction distribution in the central slice of the gasifier for different diameters of the dense-phase zone's enlarged section.

top of the rare-phase zone decrease, while the mass fraction of CO_2 increases. Thus, enlarging the diameter of the expanding section of the dense-phase zone hinders coal gas generation and facilitates char conversion.

Fig. 12 displays the time-averaged distribution of axial gas components' mass fraction in the gasifier for different diameters of the dense-phase zone's expanding section. Fig. S4 of the supporting information presents the time-averaged mole fractions of each gas component at the outlet of the gasifier's cyclone separator with different diameters of the dense-phase zone's expanding section. The diameter of the dense-phase zone's expanding section impacts the distribution of gas components within the gasifier. When the diameter is expanded to 0.5 m, the mass fractions of CH_4, H_2, and CO in the upper half of the rare-phase zone decrease, while the mass fraction of CO_2 increases. However, upon examining the mole fractions of each gas component at the outlet of the gasifier's cyclone separator, it is observed that the change in diameter of the expanding section of the dense-phase zone has little effect on the gas composition in the final output of the gasifier.

4.3.2. Diameter of rare-phase zone

The diameter of the rare-phase zone significantly affects the gas velocity in this zone, which is crucial to the number of fine particles discharged from the gasifier outlet. A reasonable diameter of the rare-phase zone can enhance tar quality and reduce gas dedusting load. Thus, two diameters of the rare-phase zone (i.e., 0.6 m and 0.8 m) are designed and numerically studied under the same operating conditions as the original diameter of 0.7 m. Fig. 13 and Fig. 14 display the time-averaged gas-phase z-direction velocity distribution in the gasifier and the transient particle size distribution at the top of the gasifier after the reactor reaches dynamic stability. It is evident that increasing the diameter of the rare-phase zone results in decreased gas velocity at the top and a noticeable decrease in fine particles discharge from the outlet. Therefore, an appropriate increase in the diameter of the rare-phase zone is acceptable without compromising normal gasifier operation while maintaining economic benefits for tar and coal gas production.

Fig. 15 presents the time-averaged distribution of axial gas components' mass fraction in the gasifier for different rare-phase zone diameters. Fig. S5 of the supporting information displays the time-averaged mole fractions of each gas component at the outlet of the gasifier's cyclone separator with different rare-phase zone diameters. The alteration in diameter of the rare-phase zone affects the distribution of gas mass fractions in the gasifier. When the diameter is increased to 0.8 m, the mass fractions of CH_4, H_2, and CO in the upper part of the rare-phase zone decrease, while the change in CO_2 mass fraction is not significant. However, the change in the diameter of the rare-phase zone has almost no effect on the final gas fraction output of the gasifier's

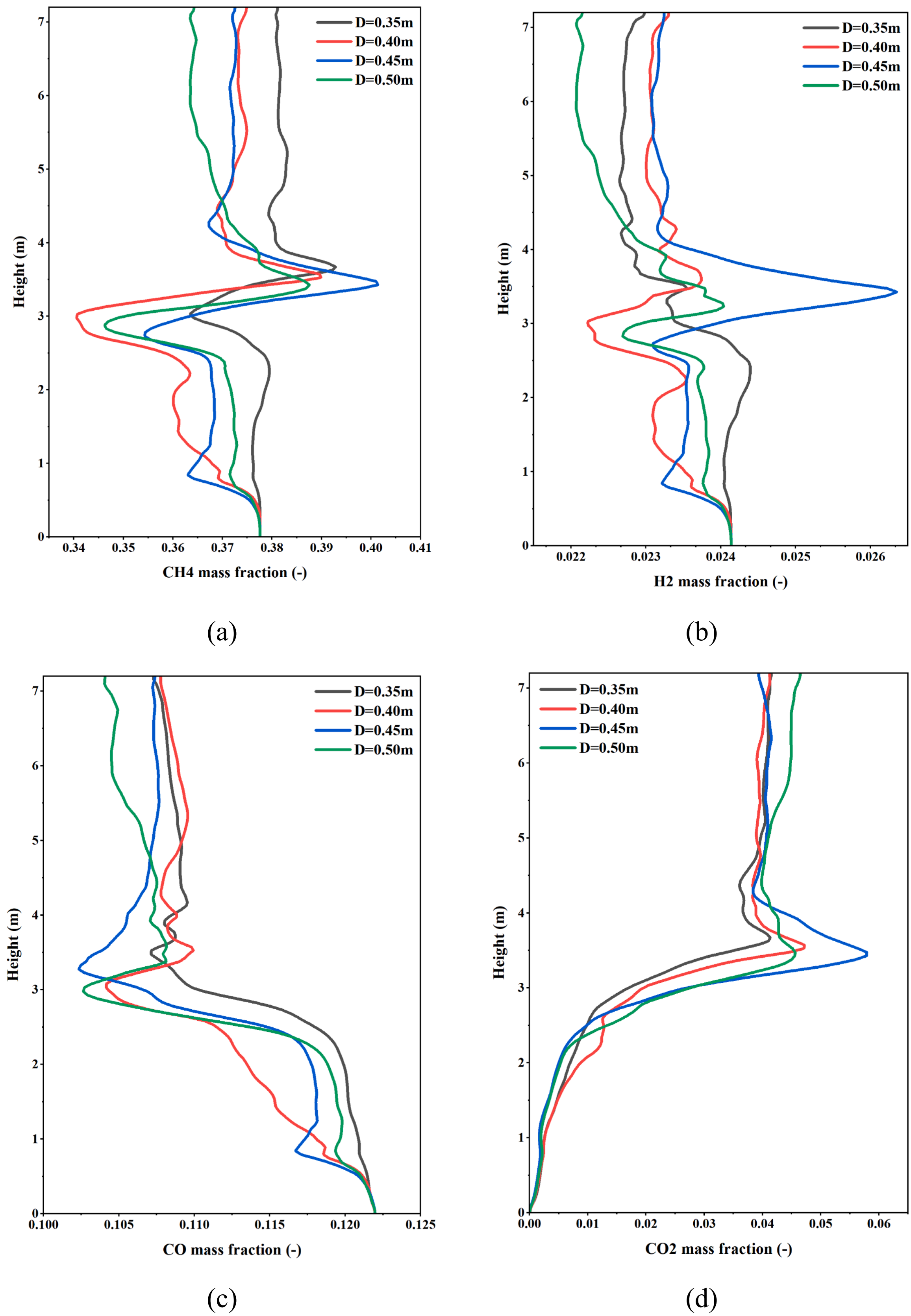

Fig. 12. Time-averaged distribution of gas components mass fraction in the gasifier axial direction for different diameters of the dense-phase zone's expanding section: (a) CH_4; (b) H_2; (c) CO; (d) CO_2.

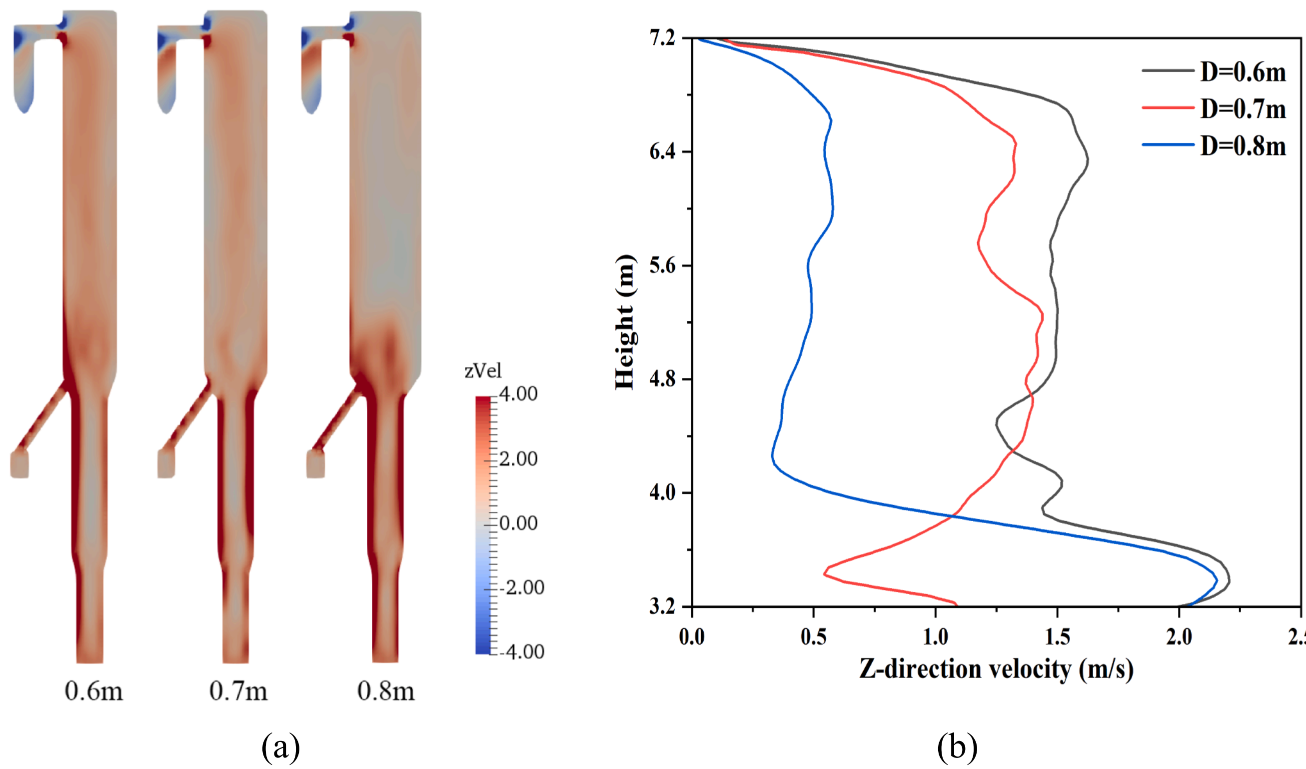

Fig. 13. Time-averaged gas-phase z-direction velocity with different rare-phase zone diameters: (a) central slice of the gasifier, (b) axial distribution along the gasifier.

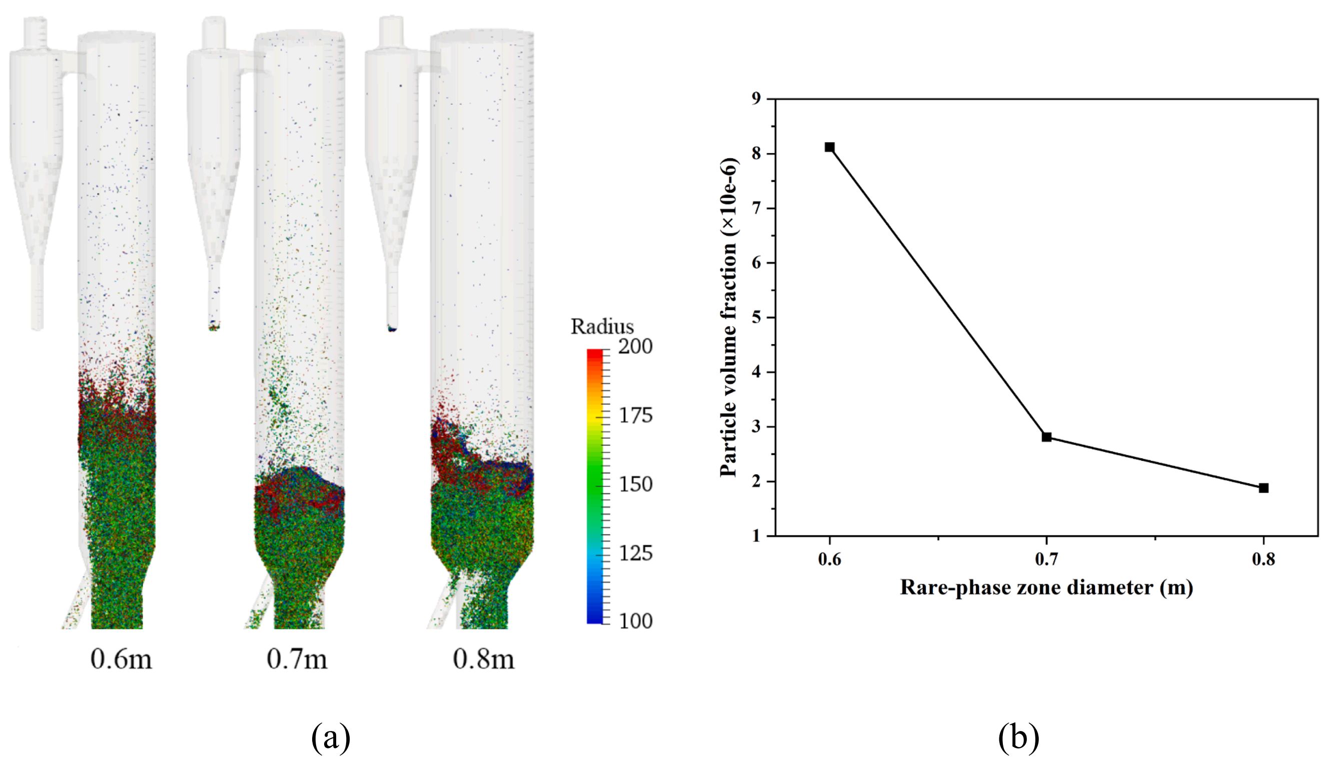

Fig. 14. (a) Transient particle size distributions at the top of the gasifier, (b) time-averaged particle volume fraction at the gasifier outlet plane for different rare-phase zone diameters.

cyclone separator.

4.3.3. Height of the rare-phase zone

The height of the rare-phase zone has a notable impact on the gas flow rate in the upper section of the gasifier. An optimal height of the

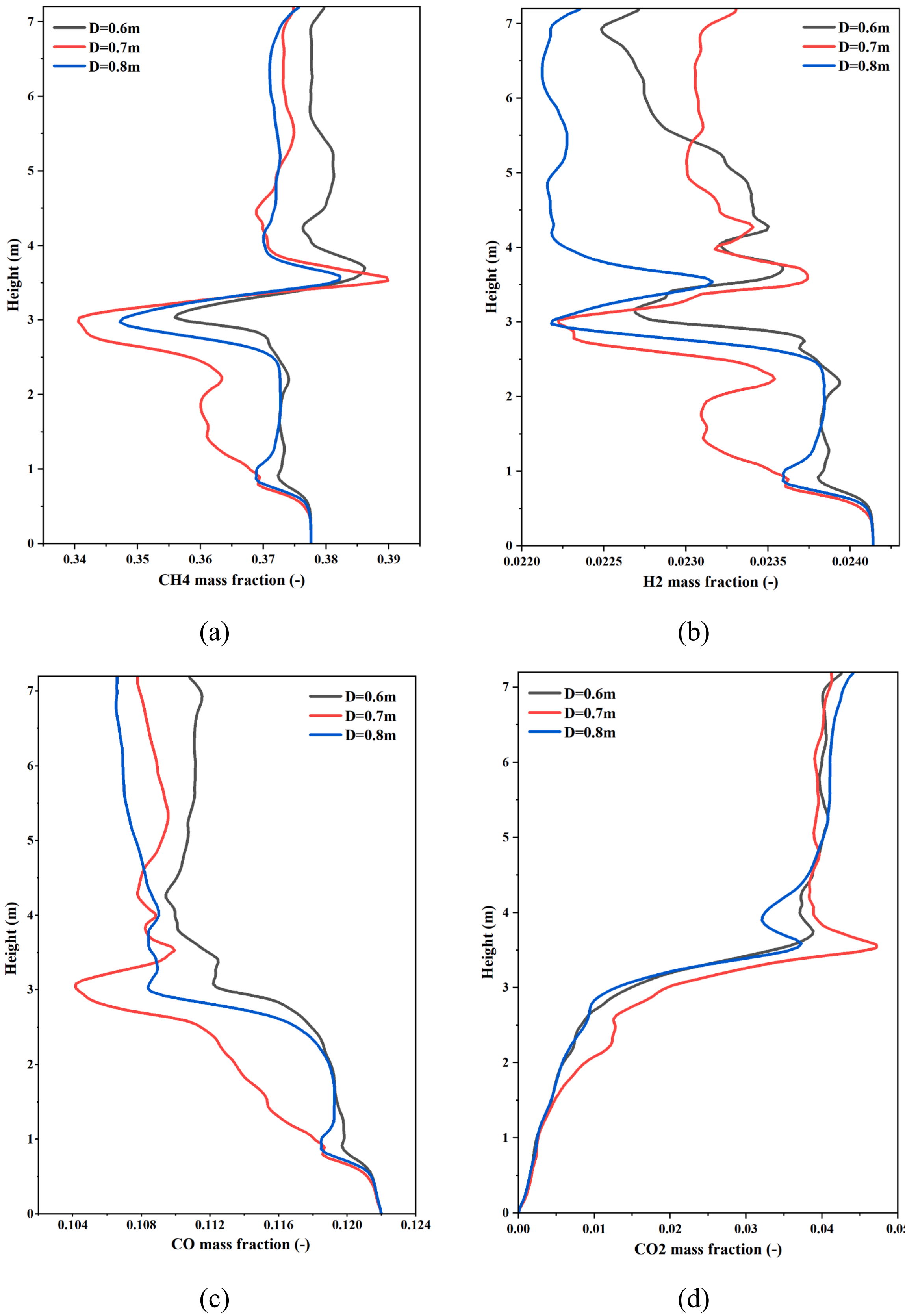

Fig. 15. Time-averaged distribution of gas components mass fraction in the gasifier axial direction for different rare-phase zone diameters: (a) CH_4; (b) H_2; (c) CO; (d) CO_2.

rare-phase zone can effectively prevent excessive fine particles from being discharged at the reactor outlet, consequently reducing the burden of dust removal in the gas stream. Fig. 5 illustrates that this region is located further away from the outlet where material particles settle and precipitate, while Fig. 9 shows a uniform distribution of gas components at the top of the rare-phase zone. Therefore, the height of the rare-phase zone can be adjusted within a specific range. In this study, two heights of the rare-phase zone are designed as 3.6 m and 4.4 m in comparison to the original height of 4.0 m. Fig. 16 presents the time-averaged distribution of particle volume fraction in the gasifier, while Fig. 17 displays the transient state of particle flow in the gasifier after dynamic stabilization. The particles at the top of the rare-phase zone were suitably distributed, with no significant particle spillage at the outlet. Therefore, based on the integration of simulation results and engineering considerations, the height of the rare-phase zone can be appropriately reduced from the original height.

Fig. 18 presents the time-averaged distribution of axial gas components' mass fraction in the gasifier for different heights of the rare-phase zone. Fig. S6 of supporting information displays the time-averaged mole fractions of each gas component at the outlet of the gasifier's cyclone separator with different heights of the rare-phase zone. The height of the rare-phase zone affects the distribution of gas mass fractions in the gasifier. Increasing the height of the rare-phase zone leads to an increase in the mass fractions of CH_4 and H_2 in the rare-phase zone, an initial increase and subsequent decrease in the mass fraction of CO, and a decrease followed by an increase in the mass fraction of CO_2. However, it has almost no effect on the final gas fraction at the outlet of the gasifier's cyclone separator.

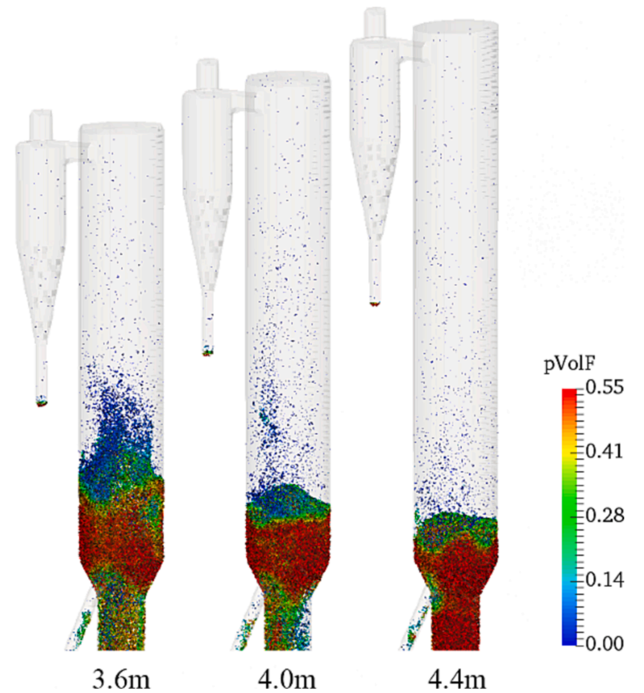

Fig. 17. Gasifier transient particle flow states for different heights of the rare-phase zone (colored by particle volume fraction).

5. Conclusions

In this work, the coal staged conversion in a 1MWth pilot-scale system is numerically studied using the MP-PIC method, which comprehensively incorporates gas–solid flow, heat and mass transfer, and chemical reaction. The model is verified to be reliable and accurate in modeling coal staged conversion in fluidized bed reactors. Then the operating mechanism and particle behavior during the staged conversion process are comprehensively discussed. Additionally, the effects of operating and structural parameters on gas–solid mixing and chemical reactions in the reactor are explored. The conclusions are as follows:

1) The operating temperature of the gasifier can significantly influence the generation of gas species. As the operating temperature increases, the CH_4 concentration at the gasifier's cyclone outlet initially rises and then declines, while the H_2 concentration decreases initially and then increases. The CO and CO_2 concentrations increase and the C_2H_6 concentration decreases. With the

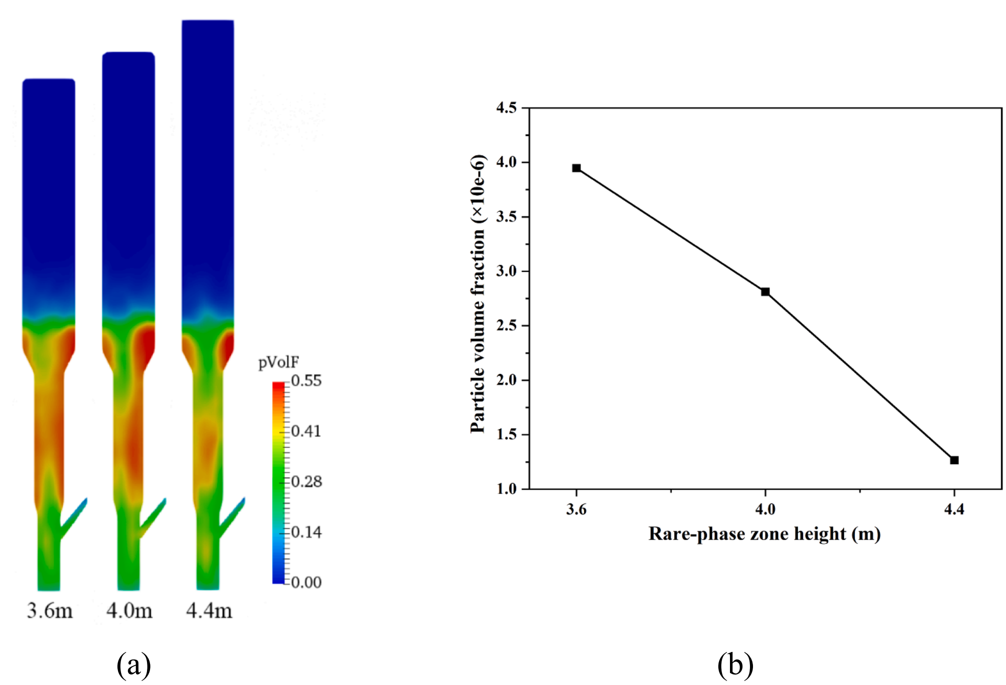

Fig. 16. Time-averaged particle volume fraction distribution for different heights of the rare-phase zone: (a) central slice of the gasifier, (b) axial distribution along the gasifier.

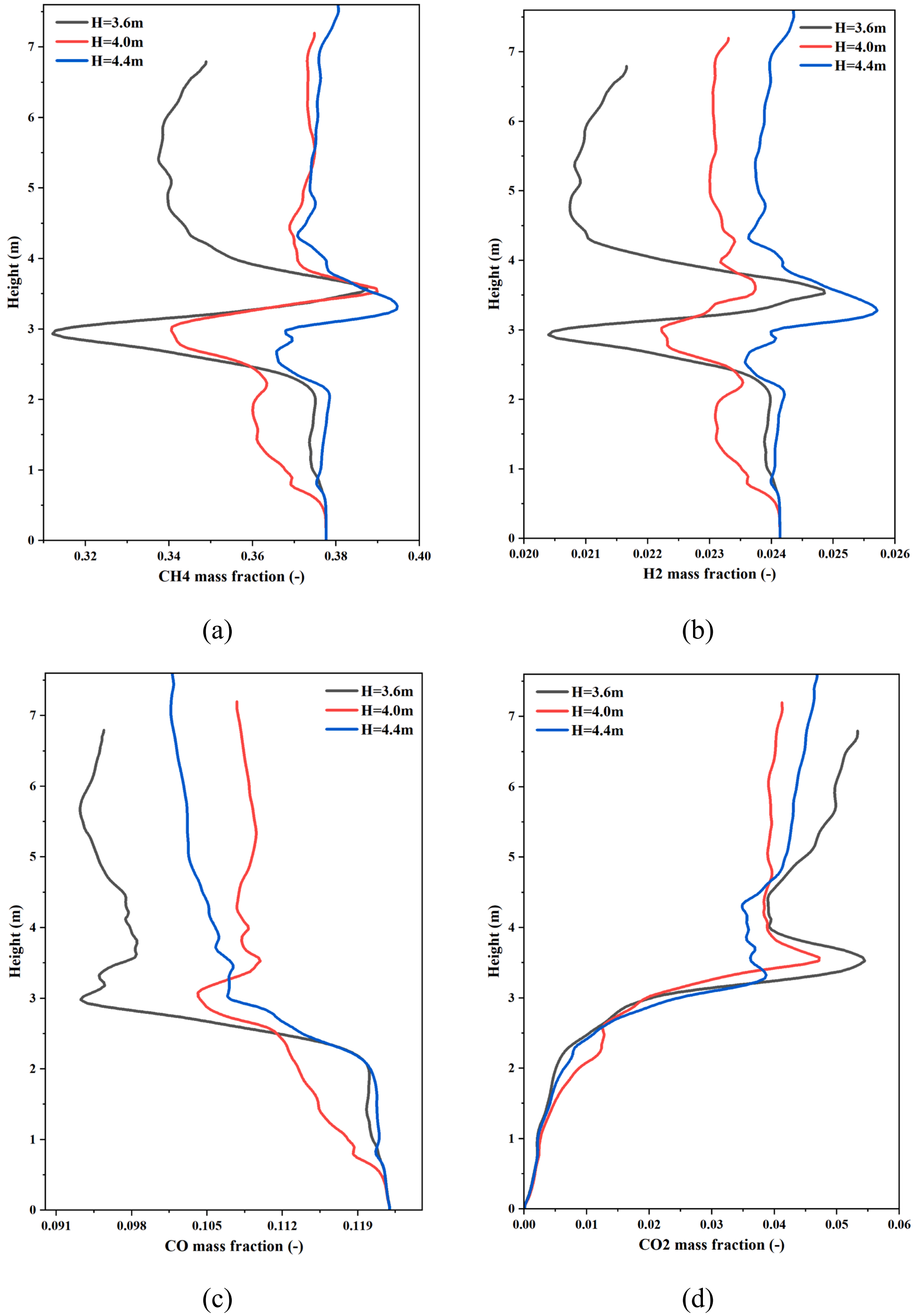

Fig. 18. Time-averaged distribution of gas components mass fraction in the gasifier axial direction for different heights of the rare-phase zone: (a) CH_4; (b) H_2; (c) CO; (d) CO_2.

increase of PSD width, the particle size distribution becomes more uneven, leading to bubbles overflowing from both sides of the bed. Consequently, the "core-annulus" structure in the expanding section of the dense-phase zone gradually disappears.

2) As the diameter of the expansion section in the dense-phase zone increases, the flow pattern in the dense-phase zone is improved, but the generation of gas in the rare-phase zone is hindered. After increasing the diameter of the rare-phase zone, the amount of fine particles carried out at the exit of the gasifier is significantly reduced. Appropriately reducing the height of the rare-phase zone can enhance the engineering economy without causing the overflow of fine particles. The variation in structure size has minimal impact on the gas fraction at the outlet of the cyclone separator.

This work is helpful for a better understanding of hydrodynamics and thermochemical characteristics of the coal staged conversion in the CFB.

CRediT authorship contribution statement

Yuxin Ge: Writing – original draft, Validation, Software. **Jiahui Yu:** Writing – review & editing. **Junjie Lin:** Methodology, Validation, Writing – review & editing. **Shuai Wang:** Writing – review & editing. **Kun Luo:** Writing – review & editing, Project administration. **Qinhui Wang:** Project administration, Resources. **Jianren Fan:** Resources, Project administration.

Declaration of competing interest

The authors declare that they have no known competing financial interests or personal relationships that could have appeared to influence the work reported in this paper.

Data availability

The data that has been used is confidential.

Acknowledgments

We are grateful for the support from the National Natural Science Foundation of China (No. 51925603) and the Fundamental Research Funds for the Central Universities (2022ZFJH004).

Appendix A. Supplementary data

Supplementary data to this article can be found online at https://doi.org/10.1016/j.cej.2024.149524.

References

[1] BP, Energy, statistical review of world, Corporation B. P., 2023.
[2] N.B.O. Statistics, China statistical yearbook-2022 (general no. 41), no. 41, China Statistics Press Ltd, 2022.
[3] M. Ahmad, M. Yousaf, J. Han, S. Ur Rahman, H. Muhammad Adeel Sharif, L. Wang, Z. Tang, Y. Zhou, Y. Huang, State-of-the-art analysis of the fuel desulphurization processes: perspective of co2 utilization in coal biodesulphurization, Chem. Eng. J. (2023) 147517.
[4] S. Wang, H. Lu, F. Zhao, G. Liu, Cfd studies of dual circulating fluidized bed reactors for chemical looping combustion processes, Chem. Eng. J. 236 (2014) 121–130.
[5] G. Zhou, W. Zhong, A. Yu, Y. Dou, J. Yin, Experimental study on characteristics of pressurized grade conversion of coal, Fuel. 234 (2018) 965–973.
[6] V. Spallina, F. Gallucci, M.C. Romano, P. Chiesa, M.V.S. Annaland, Investigation of heat management for clc of syngas in packed bed reactors, Chem. Eng. J. 225 (2013) 174–191.
[7] W. Jia, Y. Guo, F. Guo, H. Li, Y. Li, Y. Zhang, J. Wu, C. Si, Co-combustion of carbon-rich fraction from coal gasification fine slag and biochar: gas emission, ash sintering, heavy metals evolutions and environmental risk evaluation, Chem. Eng. J. 471 (2023) 144312.
[8] L. Ren, K. Zhang, F. Wang, Y. Zhang, F. Yang, F. Cheng, Microwave heating of coal slime based on multi-physics field simulations: regulating waveguide port size and sample radius to improve microwave utilization efficiency, Chem. Eng. J. 470 (2023) 143975.
[9] W. Hao, L. Zhongyang, F. Mengxiang, W. Qinhui, C. Jianmeng, Numerical simulation of gas-solid flow characteristics in poly-generation bubbling fluidized bed, Thermal Power Generation. 51 (2022) 116–123.
[10] Z. Guo, Q. Wang, M. Fang, Z. Luo, K. Cen, Thermodynamic and economic analysis of polygeneration system integrating atmospheric pressure coal pyrolysis technology with circulating fluidized bed power plant, Appl. Energy. 113 (2014) 1301–1314.
[11] S. Wang, C. Hu, K. Luo, J. Yu, J. Fan, Multi-scale numerical simulation of fluidized beds: model applicability assessment, Particuology. 80 (2023) 11–41.
[12] H. Zhu, J. Zhu, Characterization of fluidization behavior in the bottom region of cfb risers, Chemical Engineering Journal (Lausanne, Switzerland 141 (2008) (1996) 169–179.
[13] J. Xu, X. Lu, W. Zhang, J. Chen, Q. Wang, Y. Chen, Q. Guo, Effects of superficial gas velocity and static bed height on gas-solid flow characteristics in a 60-meter-high transparent cfb riser, Chem. Eng. J. 334 (2018) 545–557.
[14] A.T. Harris, J.F. Davidson, R.B. Thorpe, Particle residence time distributions in circulating fluidised beds, Chem. Eng. Sci. 58 (2003) 2181–2202.
[15] F. Alobaid, N. Almohammed, M. Massoudi Farid, J. May, P. Rößger, A. Richter, B. Epple, Progress in CFD Simulations of Fluidized Beds for Chemical and Energy Process Engineering, Prog. Energy Combust. Sci. 91 (2022) 100930.
[16] Q. Tu, H. Wang, R. Ocone, Application of three-dimensional full-loop cfd simulation in circulating fluidized bed combustion reactors–a review, Powder Technol. 399 (2022) 117181.
[17] S. Wang, K. Luo, S. Yang, C. Hu, J. Fan, Les-dem investigation of the time-related solid phase properties and improvements of flow uniformity in a dual-side refeed cfb, Chem. Eng. J. 313 (2017) 858–872.
[18] M.A. van der Hoef, M. van Sint Annaland, J. Kuipers, Computational fluid dynamics for dense gas–solid fluidized beds: a multi-scale modeling strategy, Chem. Eng. Sci. 59 (2004) 5157–5165.
[19] A. Nikolopoulos, N. Nikolopoulos, A. Charitos, P. Grammelis, E. Kakaras, A. R. Bidwe, G. Varela, High-resolution 3-d full-loop simulation of a cfb carbonator cold model, Chem. Eng. Sci. 90 (2013) 137–150.
[20] W.P. Adamczyk, P. Kozoub, G. Kruczek, M. Pilorz, A. Klimanek, T. Czakiert, G. W. Cel, Numerical approach for modeling particle transport phenomena in a closed loop of a circulating fluidized bed, Particuology. 29 (2016) 69–79.
[21] Z. Hamidouche, E. Masi, P. Fede, O. Simonin, K. Mayer, S. Penthor, Unsteady three-dimensional theoretical model and numerical simulation of a 120-kw chemical looping combustion pilot plant, Chem. Eng. Sci. 193 (2019) 102–119.
[22] K. Luo, F. Wu, S. Yang, J. Fan, Cfd–dem study of mixing and dispersion behaviors of solid phase in a bubbling fluidized bed, Powder Technol. 274 (2015) 482–493.
[23] S. Yang, K. Luo, M. Fang, K. Zhang, J. Fan, Parallel cfd–dem modeling of the hydrodynamics in a lab-scale double slot-rectangular spouted bed with a partition plate, Chem. Eng. J. 236 (2014) 158–170.
[24] D.M. Snider, An incompressible three-dimensional multiphase particle-in-cell model for dense particle flows, J. Comput. Phys. 170 (2001) 523–549.
[25] Y. Tsuji, T. Kawaguchi, T. Tanaka, Discrete particle simulation of two-dimensional fluidized bed, Powder Technol. 77 (1993) 79–87.
[26] H. Zhou, G. Flamant, D. Gauthier, Dem-les of coal combustion in a bubbling fluidized bed. Part i: gas-particle turbulent flow structure, Chem. Eng. Sci. 59 (2004) 4193–4203.
[27] H.P. Zhu, Z.Y. Zhou, R.Y. Yang, A.B. Yu, Discrete particle simulation of particulate systems: theoretical developments, Chem. Eng. Sci. 62 (2007) 3378–3396.
[28] X. Shi, X. Lan, F. Liu, Y. Zhang, J. Gao, Effect of particle size distribution on hydrodynamics and solids back-mixing in cfb risers using cpfd simulation, Powder Technol. 266 (2014) 135–143.
[29] C. Chen, J. Werther, S. Heinrich, H.Y. Qi, E.U. Hartge, Cpfd simulation of circulating fluidized bed risers, Powder Technol. 235 (2013) 238–247.
[30] Z. Yang, Y. Zhang, A. Oloruntoba, J. Yue, Mp-pic simulation of the effects of spent catalyst distribution and horizontal baffle in an industrial fcc regenerator. Part i: effects on hydrodynamics, Chem. Eng. J. 412 2021 128634.
[31] Z. Yang, Y. Zhang, T. Liu, A. Oloruntoba, Mp-pic simulation of the effects of spent catalyst distribution and horizontal baffle in an industrial fcc regenerator. Part ii: effects on regenerator performance, Chem. Eng. J. 421 2021 129694.
[32] J. Xie, W. Zhong, Y. Shao, Q. Liu, L. Liu, G. Liu, Simulation of combustion of municipal solid waste and coal in an industrial-scale circulating fluidized bed boiler, Energy Fuels. 31 (2017) 14248–14261.
[33] N.A. Patankar, D.D. Joseph, Modeling and numerical simulation of particulate flows by the Eulerian-Lagrangian approach, Int. J. Multiphase Flow. 27 (2001) 1659–1684.
[34] S. Karimipour, T. Pugsley, Application of the particle in cell approach for the simulation of bubbling fluidized beds of Geldart A particles, Powder Technol. 220 (2012) 63–69.
[35] S. Clark, D.M. Snider, J. Spenik, CO2 Adsorption loop experiment with Eulerian-Lagrangian simulation, Powder Technol. 242 (2013) 100–107.
[36] J. Xie, W. Zhong, B. Jin, Y. Shao, Y. Huang, Eulerian-Lagrangian method for three-dimensional simulation of fluidized bed coal gasification, Adv. Powder Technol. 24 (2013) 382–392.
[37] D. Yuanyuan, Z. Wenqi, Z. Guanwen, L. Qian, Y. Junping, Characteristics of gas and oil production in low temperature coal pressurized pyrolysis, J. Southeast University (natural Science Edition). 48 (2018) 85–91.
[38] G. Zhou, W. Zhong, A. Yu, J. Xie, Simulation of coal pressurized pyrolysis process in an industrial-scale spout-fluid bed reactor, Adv. Powder Technol. 30 (2019) 3135–3145.

[39] F. Meiyan, L. Fei, Effect of different bubbling bed height on particle distribution in multi - stage gasifier, Journal of Chongqing University of Technology(Natural Science). 33 2019 7.
[40] A. Sharma, S. Wang, V. Pareek, H. Yang, D. Zhang, Multi-fluid reactive modeling of fluidized bed pyrolysis process, Chem. Eng. Sci. 123 (2015) 311–321.
[41] Q. Ma, F. Lei, X. Xu, Y. Xiao, Three-dimensional full-loop simulation of a high-density CFB with standpipe aeration experiments, Powder Technol. 320 (2017) 574–585.
[42] S. Yang, F. Fan, Y. Wei, J. Hu, H. Wang, S. Wu, Three-dimensional MP-PIC simulation of the steam gasification of biomass in a spouted bed gasifier, Energy Convers. Manage. 210 (2020) 112689.
[43] Z. Guanwen, Z. Wenqi, Y. Aibing, Three-dimensional numerical simulation of fast pyrolysis of coal in pressurized spout-fluid bed, J. University Chinese Acad. Sci. 037 (2020) 210–219.
[44] S.E. Harris, D.G. Crighton, Solitons, solitary waves, and voidage disturbances in gas-fluidized beds, J. Fluid Mech. 266 (1994) 243.
[45] D.M. Snider, S.M. Clark, P.J. O'Rourke, Eulerian–lagrangian method for three-dimensional thermal reacting flow with application to coal gasifiers, Chem. Eng. Sci. 66 (2011) 1285–1295.
[46] R.J. Hill, D.L. Koch, A.J.C. Ladd, Moderate-reynolds-number flows in ordered and random arrays of spheres, J. Fluid Mech. 448 (2001) 243–278.
[47] N. Yang, W. Wang, W. Ge, L. Wang, J. Li, Simulation of heterogeneous structure in a circulating fluidized-bed riser by combining the two-fluid model with the emms approach, Ind. Eng. Chem. Res. 43 (2004) 5548–5561.
[48] J. Li, Particle-fluid two-phase flow: the energy-minimization multi-scale method, Metallurgical Industry Press (1994).
[49] H. Yoon, J. Wei, M.M. Denn, A model for moving-bed coal gasification reactors, Aiche J. 24 (1978) 885–903.
[50] W.P. Jones, R.P. Lindstedt, Global reaction schemes for hydrocarbon combustion, Combust. Flame. 73 (1988) 233–249.
[51] F. Bustamante, R.M. Enick, A.V. Cugini, R.P. Killmeyer, B.H. Howard, K. S. Rothenberger, M.V. Ciocco, B.D. Morreale, S. Chattopadhyay, S. Shi, High-temperature kinetics of the homogeneous reverse water–gas shift reaction, Aiche J. 50 (2004) 1028–1041.
[52] F. Bustamante, R.M. Enick, R.P. Killmeyer, B.H. Howard, K.S. Rothenberger, A. V. Cugini, B.D. Morreale, M.V. Ciocco, Uncatalyzed and wall-catalyzed forward water–gas shift reaction kinetics, Aiche J. 51 (2005) 1440–1454.
[53] J. Yan, X. Lu, R. Xue, J. Lu, Z. Liu, Validation and application of cpfd model in simulating gas-solid flow and combustion of a supercritical cfb boiler with improved inlet boundary conditions, Fuel Process. Technol. 208 (2020) 106512.
[54] L. Xiaohuan, Y. Shiliang, X. Qingang, H. Jianhang, Numerical simulation of coal gasification process in bubbling fluidized bed based on the mp-pic method, J. Eng. Thermophys. 44 (2023) 2161–2166.